FACULTY OF SCIENCE
UNIVERSITY OF COPENHAGEN

Optical studies of membrane-peptide interactions

Maria Christiansen

Supervisor: Lene Oddershede, Niels Bohr Institute
External supervisor: Thomas Hønger Callisen, Novozymes A/S

A Thesis Presented for the Degree of
Cand. Scient. in Biophysics

Niels Bohr Institute
University of Copenhagen
Denmark

July 1, 2008

Abstract

The purpose of this thesis is to study the interactions between different antimicrobial peptides and the outer membrane of *Escherichia coli*. Tethers are pulled from the membrane of *E. coli* bacteria by means of optical tweezers. As optical tweezers enable the measurement of forces and distances in the order of pN and nm, the visco-elastic properties of the tethers can be investigated. By pulling tethers both in the presence and absence of different antimicrobial peptides, the effect of these peptides on the outer membrane properties can be measured.
Force-extension measurements as well as relaxation measurements have been carried out in the presence of two antimicrobial peptides, arenicin-3 and a novispirin variant. None of the peptides showed any effect on the force-extension relations of the membrane tethers, while arenicin-3 was found to influence the relaxation time of the relaxation measurements.

The Niels Bohr Institute, Copenhagen - DK
July 1, 2008

Maria Christiansen
07 06 82 - 22 24

Acknowledgments

This thesis is the result of the work I have done in the Optical Tweezers group at the Niels Bohr Institute during the last year. In this time I have met many extremely pleasant people, both in the OT group, in the C-room and at the B-floor, who have all helped me in my work, either by answering my questions or by keeping my spirits up.

Of these, I would especially like to thank my supervisor Lene Oddershede for her patience and willingness to help and for letting me into a great group. I also want to thank Liselotte Jauffred, who has been an invaluable help in every difficult situation I have faced. I am very grateful that she would share her knowledge and experience.

Benedicte Mengel has very kindly let me share her office and listened to my complaints and triumphs, and she, Jonas Olsson, Katja Skaanning, and Fabian Czerwinski are all thanked for their proof-reading and questions.

Finally I would like to thank my boyfriend, friends and family for their interest and support.

Table of Contents

Chapter 1

Introduction

Antibiotic resistance is a growing health problem, as it becomes more and more difficult to treat diseases induced by bacteria. Therefore, there is an urgent need to develop new drugs against multi-resistant micro-organisms. Antimicrobial peptides, both naturally occurring and synthetic, have proven very useful in this respect, as they very efficiently attack and kill even multi-resistant bacteria. In order to optimise their structure, it is very important to know exactly how the different antimicrobial peptides attack for example *E. coli* bacteria. The purpose of this thesis is to test the effect of three different antimicrobial peptides on the outer membrane of *E. coli* bacteria. This is done by pulling tethers, small membrane tubes, from the bacteria in the presence of peptides to see if the peptides change the tether properties. A negative and positive result alike can be useful for further improvements of the peptides.

Tethers are pulled by means of optical tweezers, an instrument using a focused laser beam to trap micron-sized particles. Optical tweezers are an outstanding tool for manipulating biological specimens through their ability to measure forces and distances in the piconewton and nanometer regimes without harming living cells. As optical tweezers cannot seize the bacterial membrane directly, microscopic beads are used as handles. A bead is attached to the outer membrane of a bacterium and by trapping the bead with the optical tweezers and moving the bacterium away from the stationary trap, a visco-elastic tether is created (fig. 1.1). The tether is too small to be seen in the microscope, but the photo sequence in figure 1.2 shows what it looks like when a tether is pulled from a bacterium. When the laser is turned off, the tether retracts the bead to the bacterium like a rubber band.

Two types of experiments have been performed, namely force-extension measurements and relaxation measurements. In force-extension measurements, the tether is pulled to a certain length and then immediately retracted while the force is measured. In relax-

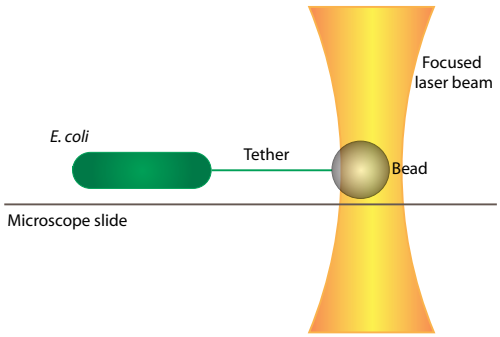

Figure 1.1: A membrane tether is formed by attaching a bead to the outer membrane of a bacterium. The bead is trapped with a pair of optical tweezers and the bacterium is moved away from the stationary trap.

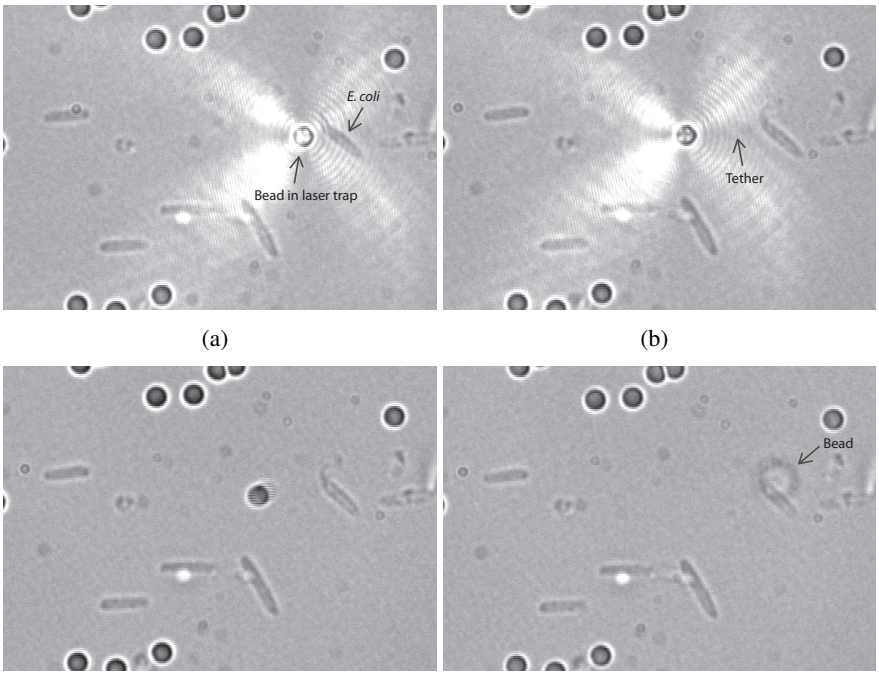

Figure 1.2: Photo sequence picturing a tether being pulled from a bacterium. In a), a bead stuck to a bacterium is captured with the optical tweezers. In b), the bacterium is moved away from the stationary trap, and a tether is created between the bead and the bacterium. In c), the laser is turned off, and because the bead is no longer trapped, it is pulled back towards the bacterium by the tether. In d), the bead has reached the bacterium again.

ation measurements, the tether is pulled to a certain length and held there for approximately 280 seconds. The force-extension measurements give a linear correlation between the force needed to pull the tether and the distance it is extended which obeys Hooke's law $F = \kappa_t \cdot x$. The value of κ_t gives the spring constant for the tether, thereby showing its elastic properties. The relaxation measurements display a Maxwell-like exponential decrease in the force reflecting the viscous properties of the tether.

By conducting these two types of measurements both in the presence and absence of peptide and comparing the results, it is seen that the peptides have no influence on the spring constant of the tethers while the relaxation appears to be affected.

1.1 Outline

The thesis can be divided into three main parts. The first part forms the biochemical basis necessary for an understanding of peptide-membrane interactions and consists of chapters 2, 3, and 4. Chapter 2 introduces the bacterium *Escherichia coli*, chapter 3 describes a supposed model for the action mechanism of antimicrobial peptides and introduces the peptides used in this thesis, and chapter 4 describes some general properties of membrane tethers.

The second part, consisting of chapters 5 and 6, describes the main aspects of the theory behind optical trapping as well as the optical tweezers setup employed in my work.

The last part contains chapters 7, 8, and 9, and is the main part of the thesis. Here, the experimental procedure with regard to sample preparation and data acquisition is described and the experimental results are presented and discussed.

Detailed protocols for the sample preparation can be found in appendix A and recipes are listed in appendix B.

Chapter 2

Escherichia coli

All experimental work in this thesis is done on the bacterium *Escherichia coli*, as it is easy to grow and genetically manipulate, and I will therefore give a short introduction to the organism. This chapter is mainly concerned with the structure of the outermost membrane of the bacterium, as optical tweezers can only investigate this part of the membrane.

2.1 *E. coli Bacteria*

E. coli is a rod-shaped bacterium approximately 2 μm long (fig. 2.1).

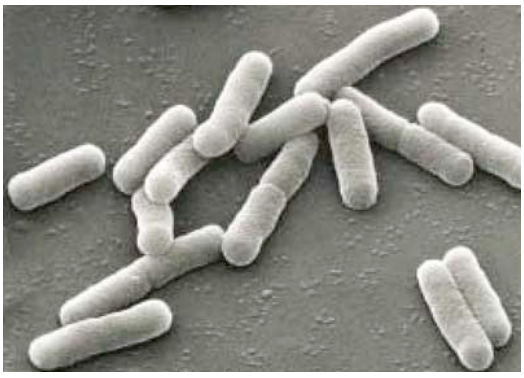

Figure 2.1: Scanning electron micrograph of *E. coli* bacteria. Picture taken from [*http://www.abpi.org.uk/publications/publication_details/targetCrohns/QA.asp*].

It is found in the lower intestine of warm-blooded animals, where it facilitates the uptake of nutrients. Furthermore it produces vitamin K_2 [1] and thereby helps prevent vitamin K-deficiency in the host. It is a facultative anaerobic organism, meaning that it produces ATP by aerobic respiration if oxygen is present and by fermentation if in

anaerobic conditions. Normally, *E. coli* bacteria are harmless, but certain virulent strains can cause infections of the gastrointestinal and urinary tract.

2.1.1 Biochemical properties

E. coli belongs to the group of Gram-negative bacteria. These bacteria are enclosed by an outer and an inner membrane separated by a stiff layer of peptidoglycan. The peptidoglycan layer consists of polymers of sugar and amino acids and forms a mesh-like structure approximately 7-8 nm thick [2]. The outer membrane consists of one leaflet of negatively charged lipopolysaccharides (LPS) held together by Mg^{2+} and Ca^{2+} from the extra-cellular medium, and one leaflet of phospholipids. The inner membrane, also called the cytoplasmic membrane, consists of a lipid bilayer similar to that surrounding eukaryotic cells (fig 2.2b). The LPS layer in the outer membrane protects the bacterium against chemical attacks. LPS also triggers the immune system of animals by binding to the CD14/TLR4/MD2 receptor complex. LPS is composed of 3 domains, namely lipid A, core LPS and O antigen (fig. 2.2c).

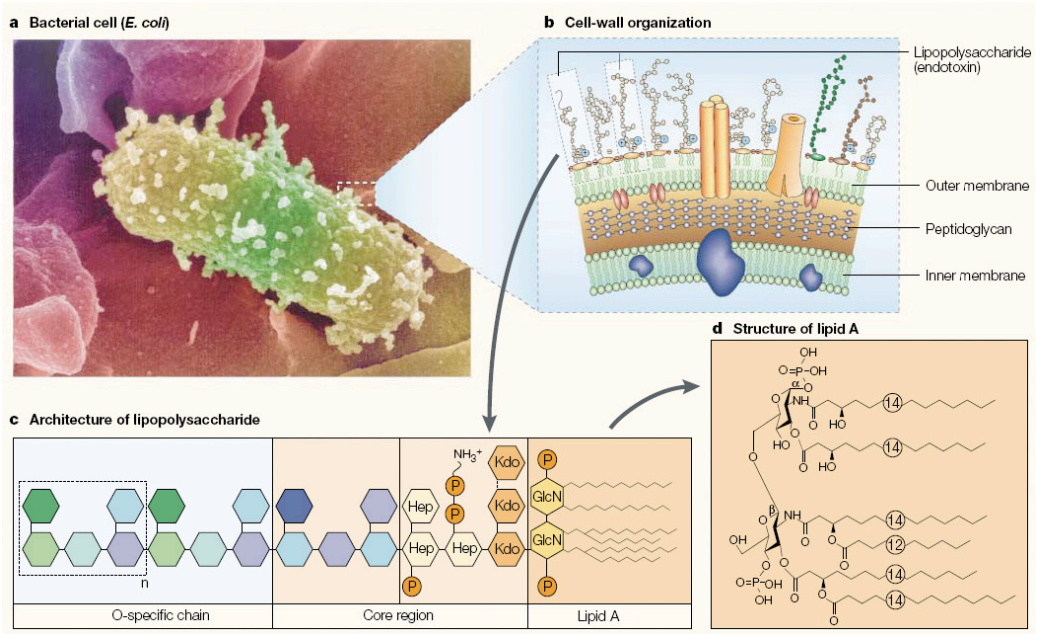

Figure 2.2: Membrane structure of *E. coli*. a) Electron micrograph of an *E. coli* bacterium. b) Schematic representation of the cell wall. c) Composition of LPS. d) Structure of the lipid A part of the LPS. GlcN: D-glucosamine; Hep: L-glycero-D-manno-heptose; Kdo: 2-keto-3-deoxy-octulosonic acid; P: Phosphate. Figure from [3].

Lipid A The lipid A present in *E. coli* bacteria consists of an N-acetylglucosamine (carbohydrate) dimer containing a phosphate group on each carbohydrate. Furthermore the dimer contains 6 acyl chains (fatty acids). Four of the chains are C14 β-hydroxy acyl chains of which two are attached to each of the two sugars. The last two chains are attached to the β-hydroxy groups of two of the C14 chains and are a C12 and a C14 chain, respectively (fig. 2.2d).

Lipid A is hydrophobic and anchors the LPS to the outer membrane. Furthermore, lipid A is responsible for many of the immune activating abilities of LPS [4].

Core LPS The core region of LPS can be divided in two sub-domains, namely the inner and the outer core, as seen in figure 2.2c. The inner core contains heptose and KDO (2-keto-3-deoxyoctulosonic acid), and the outer core is composed of different sugars depending on the strain.

O-angtigen The O-angtigen also consists of polysaccharides, but the composition varies between different strains of Gram-negative bacteria. It can consist of up to 40 repeating units containing up to 7 different sugars. Furthermore, as O side chains are easily recognised by antibodies in the host immune system, a variation of the O-antigen can also be used to avoid detection.

Chemotypes

Different mutants of *E. coli* are able to synthesise different parts of the LPS layer mentioned and thereby become different chemotypes. The *E. coli* mutants able to synthesise all parts of the LPS layer are called smooth. Mutants missing parts or all of the O antigen are called rough, and mutants missing the outer core as well as the O-antigen are called deep rough.

Most bacteria can form pili, hair-like threads, which they use to adhere to solid surfaces in order to move around. Pili can also be used to promote bacterial conjugation, which is a process where DNA is transferred from one bacterium to another. The pili used for conjugation are called sex-pili and a normal bacterium have 1-4 of these on the surface together with 100-200 common pili [5]. The strain used in this thesis has been genetically modified so that it cannot form pili.

Chapter 3

Antimicrobial Peptides

This chapter will give an introduction to antimicrobial peptides and their supposed mechanisms of action. The mechanisms will later be used to understand how the three peptides investigated in this thesis might influence the outer membrane of *E. coli* bacteria.

3.1 General Properties

Antimicrobial peptides (AMPs) are small molecules composed of approximately 20-40 amino acids. AMPs are produced by all multi-cellular organisms so far investigated [6], including humans and plants, and act as a fast supplement to the pathogenic immune response. This is important because the other components of the innate immune response are slow compared to microbial proliferation[1].

Different antimicrobial peptides attack a wide variety of cells, i.e. one peptide does not show affinity towards only one group of pathogens. The diversity of the AMPs discovered so far is so outspoken that the same peptide sequence is rarely found in two different animal species, even if they are closely related [8]. This diversity arises because single mutations can considerably alter the biological activity of each peptide. In spite of this, antimicrobial peptides have some common properties. Most peptides are cationic due to the presence of several lysine and arginine residues and contain spatially separated hydrophobic and charged regions [8], thus being amphipathic. As a result, many AMPs form amphipathic secondary structures such as α-helices and β-sheets upon contact with a cell membrane [7].

Microbial organisms have demonstrated a surprising disability of developing resistance against antimicrobial peptides. This lack of resistance must mean that the AMPs

[1]The doubling time for *E. coli* is 20 min under optimal growth conditions [7].

target a design feature which is an important and conserved component of the microbes that cannot be altered. This component has turned out to be the cellular membrane of the invading organisms. The mechanism of action is not only very efficient against microbes, it also enables a very important discrimination between hostile cells and self, as eukaryotic and prokaryotic cells have very different cell membrane compositions. These characteristics make antimicrobial peptides very interesting from a pharmaceutical point of view, as especially bacterial resistance is a growing problem with regard to conventional antibiotics.

In the next section, I will review the Shai-Matsuzaki-Huang model for the membrane attacking mechanism which is thought to describe the action of the peptides. I will only focus on the part of the model concerned with peptide-bacteria interactions, in particular Gram-negative bacteria, as this is the one of interest to the present thesis.

3.2 Mechanisms of action

A generally accepted model for the activity of antimicrobial peptides is the Shai-Matsuzaki-Huang (SMH) model [6], [7], [9]. In the model, cationic antimicrobial peptides interact with the bacterial membrane causing a displacement of lipids subsequently altering the membrane structure. As a result, the bacterial membrane is permeabilised or disrupted and the bacterium is killed.

3.2.1 Attachment

The first step in the attack is the attachment of peptides to the outer cell membrane, which according to the model occurs mainly due to electrostatic interactions. As mentioned in section 2.1, the outermost leaflet of *E. coli* consists of polyanionic LPS held together by magnesium and calcium ions. The cationic peptides have been shown to have a higher affinity for LPS than the ions [10]. Therefore, the peptides displace the ions and associates with the LPS. In comparison, the outer leaflet of mammalian cell membranes is composed of phospholipids with no net charge, and thus no electrostatic interactions occur. As antimicrobial peptides are not just completely positively charged but also contain hydrophobic regions, there are some hydrophobic interaction between non-polar amino acids in the peptides and the hydrophobic core in the membrane (fig. 3.1), but the hydrophobic interactions alone are generally too weak to lead to association. The cationic peptides will therefore only interact with the bacterial membranes and leave the host cells unharmed, and thus a way of discriminating between bacteria and mammalian cells has occurred.

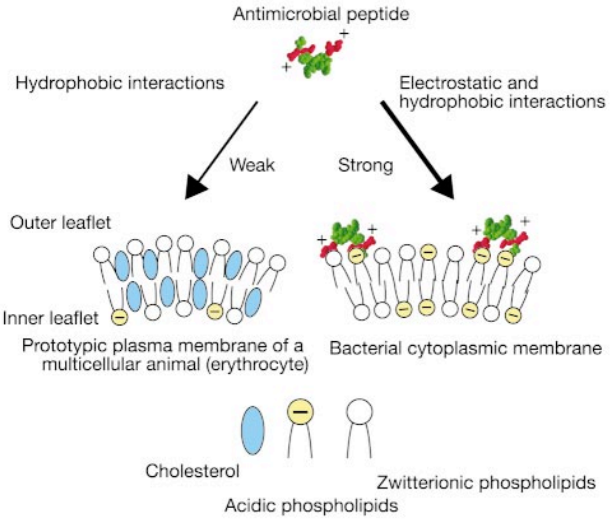

Figure 3.1: Molecular basis for binding and membrane discrimination by antimicrobial peptides. Positively charged antimicrobial peptides associate with the negatively charged bacterial membrane but not with the neutral eukaryotic membrane [8].

Several experiments support the suggested mechanism for attachment described here. For example, experiments on peptide activity have been done with both L-enantiomers and D-enantiomers, where both enantiomers showed the same activity. If the binding had been due to stereo-specific protein receptors, which is the most probable other binding mechanism, the two different orientations of the peptides would have influenced membrane-peptide association and thereby peptide activity [11], [12]. Furthermore, experiments with binding of cationic peptides to an anionic membrane in the presence of salts have been conducted [13]. These experiments reveal that adding salt to the membrane-peptide solution in some cases hinders complex formation because the salt screens the charges.

3.2.2 Association

Upon attachment to the bacterial cell membrane, the still unfolded peptides are proposed to translocate the outer membrane in a process called self-promoted uptake [10]. The peptides are suggested to neutralise the charge over an area of the outer membrane upon association. As a result, cracks are created through which the peptides can cross the outer membrane and access the cytoplasmic membrane. No explanation of how the peptides cross the peptidoglycan layer is found in the literature, but a possible mechanism could be the same as for the outer membrane. Parts of the peptidoglycan layer are positively

charged, and as the layer is mesh-like, it might be easy for the peptides to form holes large enough to pass through. When the peptides reach the acidic phospholipid bilayer constituting the cytoplasmic membrane, they most likely assume their secondary structure [7]. Some β-sheet peptides, however, might already have their secondary structure in aqueous solution because of the stabilising disulphide bridges forming the basis for the structure, and evidence exists that the interaction with lipid A can induce helix formation for α-helical peptides [12]. After association with the outer monolayer of the inner membrane, there is a divergence in the mechanisms of action depending on the type of association. These mechanisms cannot be studied experimentally in this thesis, as optical tweezers can only be used to investigate properties of the outer membrane of the bacteria. However, I will shortly describe the different processes in order to complete the picture of the action of antimicrobial peptides.

In vitro studies show that peptides associate with membranes in two distinct states depending on the peptide/lipid (P/L) ratio [9]. At low P/L, approximately 1/100 [7], both α-helical and β-sheet peptides are associated with the head groups of the lipid bilayer. This state is functionally inactive and is called the surface state (S). In the S state, the peptides are arranged parallel to the interface [9]. The incorporation of peptides into the bacterial membrane causes a positive strain in the lipid bilayer because the outer leaflet is stretched compared to the inner leaflet. As the embedded peptides push the lipid polar head groups aside, a gap is formed in the membrane. In order to fill the gap, the membrane locally becomes thinner (fig. 3.2) [14].

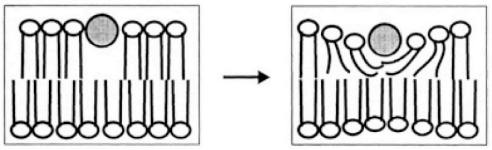

Figure 3.2: The incorporation of a peptide into the head group region of the outer monolayer of the cytoplasmic membrane leads to gap formation (*left*). For the gap to be filled, the membrane becomes locally thinner (*right*). Figure modified from [14].

The membrane thickness decreases almost linearly with increasing peptide concentration [14]. As the membrane deformation free energy increases quadratically with the change in thickness, and the thickness is almost proportional to the concentration, the free energy of the membrane increases roughly with the square of the peptide concentration. This means that the peptide molecules remain on the surface of the membrane until a certain threshold concentration P/L* is reached. Below P/L*, the binding energy and the free

energy of compression is lower than the energy of insertion. As P/L* is reached, however, it starts to be favourable for the peptides to adopt a transmembrane orientation, and thus the peptides become inserted into the membrane for P/L higher than P/L* [15]. This state is called the I state.

P/L* depends on many different factors such as the binding energy between peptides and membrane, the elastic constants of the bilayer, and the lipid composition of the bilayer [15].

3.2.3 Permeabilisation

Three models are proposed by the SMH model to explain peptide activity for peptide-membrane associations in the I state. These models are the barrel-stave model, the toroidal-pore model, and the carpet model. Most of the literature on the models is concerned with α-helical peptides, while less work is done with β-sheet peptides. Therefore, I will only give special examples of β-sheet peptides when they apply.

Barrel-stave model

In the barrel-stave model, peptide helices form a transmembrane pore. The only peptide seen to form this kind of pore is alamethicin [16]. Its hydrophobic regions associate with the hydrophobic core of the bilayer, and the hydrophilic regions line the lumen of the pore (fig. 3.3).

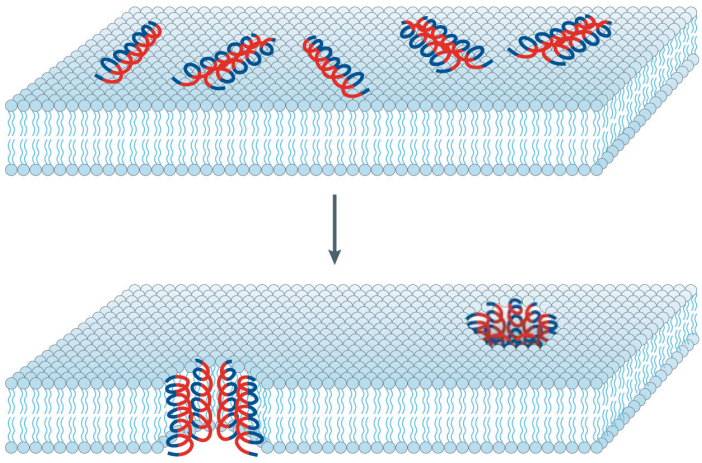

Figure 3.3: In the barrel-stave model, alamethicin peptides aggregate and insert into the membrane so that the hydrophobic regions (blue) associate with the membrane and the hydrophilic regions (red) form the interior of the pore [16].

The inner diameter of the pore is approximately 18 Å [16], which is enough to allow in- and efflux of ions.

Toroidal-pore model

This model is quite similar to the barrel-stave model, except that the lipids of the outer monolayer bend continuously through the pore so that the lumen of the pore is lined by both peptides and intercalated lipids (fig 3.4). All the way through the formation of this toroidal pore, the polar regions of the peptides are associated with the polar head groups of the lipids.

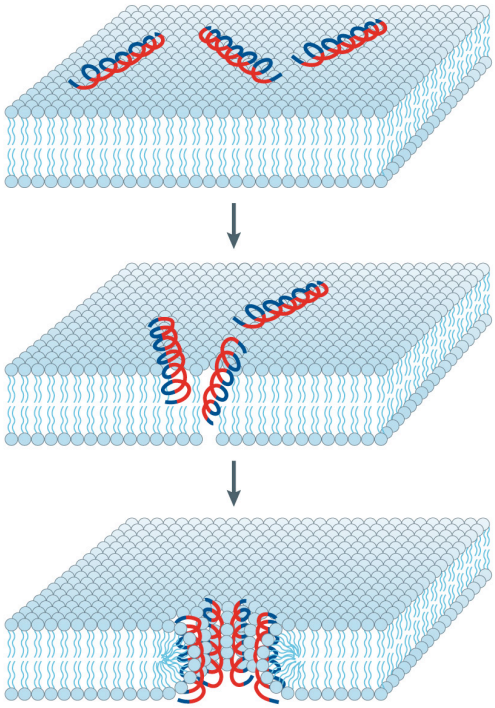

Figure 3.4: In the toroidal model, peptides aggregate and induce the lipid monolayers to bend continuously through the pore so that the aqueous lumen is lined by both peptides and lipid head groups [16]. Hydrophilic regions of the peptides are red and hydrophobic regions are blue.

As more peptides accumulate, they will repel each other. This leads to a peptide translocation to the inner monolayer after disintegration of the pores, giving the peptides access to the cytosol of the bacterium. Furthermore, the structure of the toroidal pores allows exchange of lipids between the outer and the inner monolayer. As the composition of the two monolayers is different, this might have an impact on the cell function.

The toroidal model is mainly valid for α-helical peptides, but the β-sheet peptide

tachyplesin has also been shown to form pores in liposomes followed by translocation of the peptides. It is not known if lipids are a part of the pore structure, however, or if the peptide triggers lipid exchange [7].

On the contrary, another β-sheet peptide, polyphemusin I, appears to traverse the membrane without pore formation. This peptide simply disrupts the lipid organisation and thereby translocates across the bilayer [10].

Carpet model

The mechanism of the carpet model differs from the two other models in that the peptides do not integrate into the hydrophobic core of the inner membrane. In this model, the peptides act much more like detergents. The membrane is disrupted due to a destruction of the bilayer curvature, and peptides are in contact with the lipid head groups during the whole process of membrane permeation (fig. 3.5) [6].

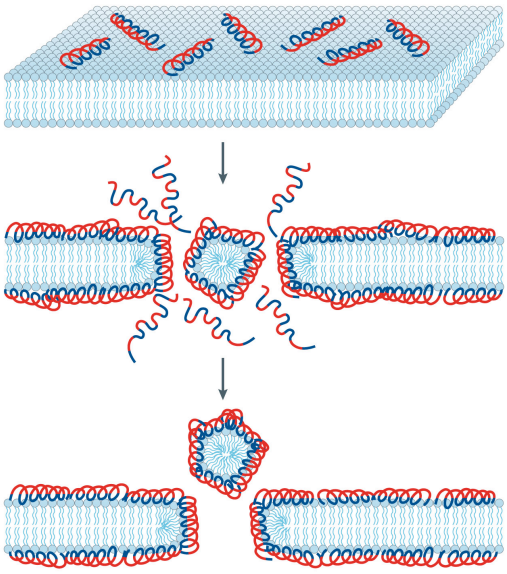

Figure 3.5: In the carpet model, peptides disrupt the membrane by covering the surface of the lipid bilayer [16]. Hydrophilic regions of the peptides are red, and hydrophobic regions are blue.

In this model, peptides do not necessarily adopt a secondary structure.

The carpet model can be seen as a high-concentration extension to the toroidal-pore model. At a certain peptide concentration, toroidal transient holes are formed in the membrane. This allows additional peptides to access the membrane, and finally the membrane disintegrates [16], [6].

The β-sheet peptide androctonin has been suggested to use the carpet mechanism when attacking *E. coli* bacteria [17]. Below are several electron micrographs (fig. 3.6) showing the effect of the peptide on the membrane of *E. coli* bacteria at different concentrations. MIC is short for minimum inhibitory concentration and corresponds to the lowest concentration of peptide needed to inhibit the growth of a given micro-organism.

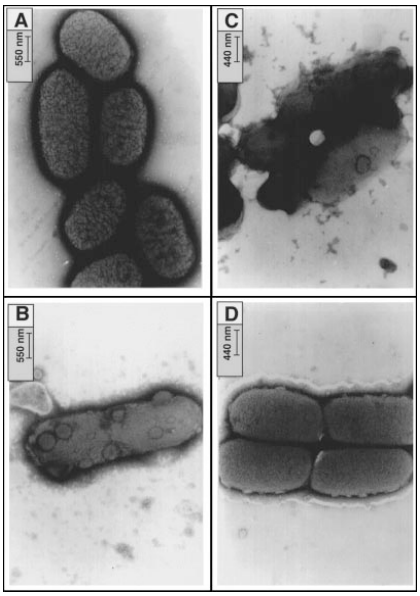

Figure 3.6: A) Control. B) *E. coli* treated with androctonin at a concentration lower than MIC. C) *E. coli* treated with androctonin at a concentration equal to MIC. D) *E. coli* treated with dermaseptin S, a naturally occurring α-helical peptide, at a concentration lower than MIC [17].

The pictures clearly show that the membrane is disrupted when the peptide concentration is high enough.

Membrane permeation by pore formation can, to a certain extent, be counter-acted by ion channels and pumps. Disruption, on the contrary, is irreversible an inevitably leads to cell death [7].

3.2.4 Cell death

Membrane disruption and the formation of pores are most likely not the only mechanisms of microbial killing. As explained above, the toroidal-pore mechanism leads to a translocation of peptides into the cytosol of the bacterium. Once the peptides have reached this region, several other mechanisms such as DNA-binding and inhibition of cell-wall synthesis might be put into play. Figure 3.7 gives an overview of these mechanisms.

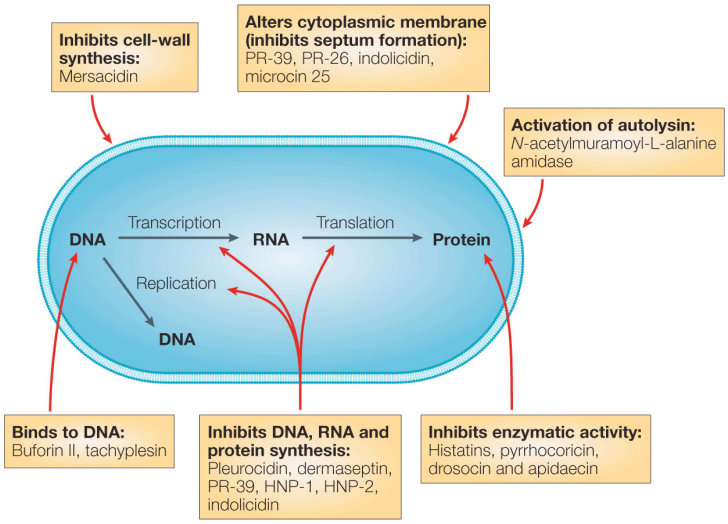

Figure 3.7: Different modes of action for intracellular antimicrobial peptide activity. The target micro-organism is an *E. coli* cell [16].

To my knowledge, the SHM model is still considered to give a valid explanation for the activity of peptides, both on the basis of experiments and theoretical models. See for example [18] and [19] for Monte Carlo simulations of the interaction between peptides and lipid bilayers. Recently, however, an extension to the model build on the detergent-like features of peptides has been presented in a review by Bechinger and Lohner [11]. This extended model is called the detergent-like model, and it describes the effect of peptide structure, membrane composition, and peptide/lipid ratio on the membrane structure in terms of a phase diagram. The model suggests that the toroidal-pore model and the carpet model described above are only special cases in this complex phase diagram. I shall not go further into detail with the detergent-like model as it does not contribute any further to the understanding of how peptides work.

The next section is concerned with a description of the peptides used in the experimental work of this thesis.

3.3 Peptides of this Thesis Work

Several factors influence the activity of peptides, for example the size of the peptide, the amino acid sequence, the overall charge, the distribution of hydrophobic and hydrophilic regions, and the structure. This means that when synthetic peptides are constructed, the

replacement of just a single amino acid with another can have great effects on the peptide activity.

The three peptides used in this thesis are plectasin, arenicin-3, and a novispirin variant, all small cationic peptides, kindly provided by Novozymes A/S. Below I will go through the properties of each peptide in as much detail as possible. It is not possible to give much information, however, as the structures of arenicin-3 and the novispirin variant are not public.

3.3.1 Plectasin

Plectasin belongs to a group of antimicrobial peptides called defensins. Defensins are small, cysteine-rich cationic proteins found in both vertebrates, invertebrates and higher plants. In humans they are found in cells of the innate immune system where they play a role in killing phagocytised bacteria, mainly by means of pore formation [13]. Due to the cysteine residues, defensins form β-sheet structures stabilised by disulphide bridges.

Plectasin is isolated from a fungus, the saprophytic ascomycete *Pseudoplectania nigrella* [20]. The peptide has shown very low toxicity against murine fibroblasts and human epidermal keratinocytes as well as human erythrocytes, and a high activity against Gram-positive bacteria with a MIC of approximately 1 μg/mL [20]. Gram-negative bacteria, on the other hand, show considerably more resistance [20]. The MIC against *E. coli* bacteria is >128 μg/ml. (Personal correspondence with P. H. Mygind, Novozymes A/S.)

Plectasin consists of 40 amino acids. The structure of plectasin, both primary, secondary and tertiary, resembles that of defensins found in spiders, scorpions, dragonflies, and mussels. Plectasin forms a tertiary structure with one α-helix and two anti-parallel β-strands stabilised by three intramolecular cysteine disulphide bridges [20]. Figure 3.8 shows the structure of plectasin visualised by the program Pymol.

3.3.2 Arenicin-3

Arenicin-3 is a synthetic β-hairpin peptide consisting of 21 amino acids. The structure shown in figure 3.9 is not arenicin-3, but the similar peptide arenicin-2, which also forms a β-hairpin.

Arenicin-3 is less cationic than plectasin and the novispirin variant, but is has a higher activity against *E. coli* bacteria with a MIC at 0.5 μg/ml. (Personal correspondence with P. H. Mygind, Novozymes A/S.)

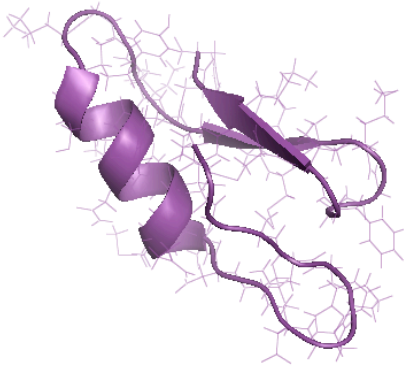

Figure 3.8: 3D structure of plectasin. The picture is a visualisation of the structure information from the Protein Data Bank (PDB). Plectasin has the PDB-ID 1zfu.

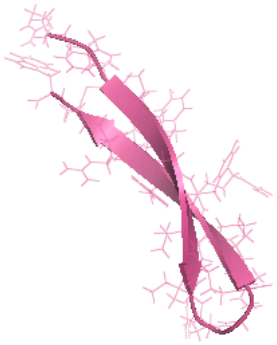

Figure 3.9: 3D structure of arenicin-2. The picture is a visualisation of the structure information from the Protein Data Bank (PDB). Arenicin-2 has the PDB-ID 2jni.

3.3.3 Novispirin variant

The novispirin variant is an α-helical peptide consisting of 18 amino acids. Like arenicin-3 it exhibits high activity against *E. coli* bacteria having a MIC of 1.5 μg/ml. (Personal correspondence with P. H. Mygind, Novozymes A/S.) The peptide resembles the novispirin variant G10 (fig. 3.10), and I will therefore use this as reference.

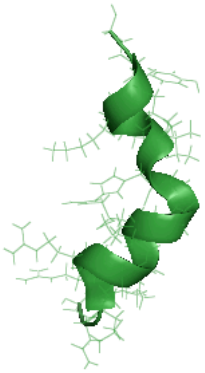

Figure 3.10: 3D structure of G10 novispirin. The picture is a visualisation of the structure information from the Protein Data Bank (PDB). G10 novispirin has the PDB-ID 1hu6.

Novispirin G10 has been shown to kill *E. coli* within 5-10 minutes [21]. This might not apply to the variant used in this thesis, though, as even small differences in structure can have a large impact on activity, as mentioned in the beginning of this section.

Experiments done with novispirin G10 [22] indicate that the peptide insert into micelles and therefore might use the pore-formation mechanism.

Table 3.1 sums up the features of the three different peptides.

Table 3.1: Features of the three peptides used for experiments.

Name	Size	Secondary structure	MIC
Plectasin	40 aa	α-helix and two anti-parallel β-sheets	>128 μg/mL
Arenicin-3	21 aa	β-hairpin	0.5 μg/mL
Novispirin variant	18 aa	α-helix	1.5 μg/mL

Chapter 4

Membrane Tethers

This chapter will give an overview of literature concerned with tether formation. A large amount of articles regarding tethers has been published, and I shall therefore only give a summary of the topics of interest to my work.

Tethers are elastic tube formations consisting of membrane material. So far, tethers have mainly been pulled from eukaryotic cells or artificial vesicles by means of optical tweezers or pipette aspiration. To my knowledge, the only work concerned with prokaryotic tethers has been done by L. Jauffred *et al.* [23]. The prokaryotic tethers resemble eukaryotic tethers in many ways, however, and therefore a brief introduction will be given to eukaryotic tethers and some factors that influence them. Thus the following sections will first give an introduction to a geometric approach to tether shape and formation by Powers *et al.* [24]. Then some properties of eukaryotic tethers and tethers pulled from artificial vesicles are outlined, and finally I will describe the model for prokaryotic tether composition suggested by L. Jauffred *et al.* [23].

4.1 Geometric Theory of Tether Formation

Powers *et al.* have made a model for tether formation based on a geometric approach [24]. The basis for the model is a classical soap film geometry. Imagine two parallel circles, one at a height h_0 above the other, connected by a soap film. The rings are slowly pulled apart, which makes the film evolve through a series of catenoids. When the ring separation reaches a critical value approximately equal to the radius of the smallest ring, the soap film breaks. In the model by Powers *et al.*, the soap film is replaced with a lipid bilayer (fig. 4.1).

The model shows that the bilayer forms catenoidal shapes just like the soap film when the ring separation is small (for a mathematical derivation see [24]). At larger separations,

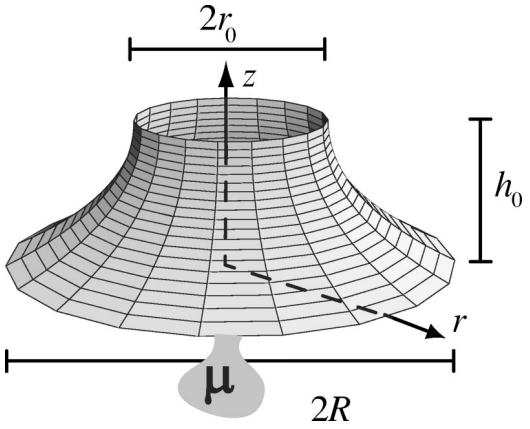

Figure 4.1: Schematics of the model problem. Two parallel rings with aligned centers are connected by a lipid bilayer membrane in contact with a lipid reservoir at fixed chemical potential per unit area μ/a [24].

however, the membrane does not break. Instead, it forms a thin cylindrical tether. This can be assigned to the elastic properties of the membrane. To better understand these properties, two examples of macroscopic elastic surfaces are reviewed, namely shells and soap films [24].

A shell is a solid surface with a small thickness and a preferred shape. The force required to bend a shell is much less than that required to stretch the shell. In other words the in-plane rigidity is much more significant than the bending rigidity. Therefore, isometric deformations of a shell, i.e. deformations where nearby points remain at a fixed distance, have the smallest energy. A nearby example from daily life is a sheet of paper, which can very easily be bent but is much harder to stretch.

The soap film has quite different properties. Since it is liquid, the static in-plane rigidity disappears. Deformations do not have to be isometric, for example illustrated by the fact that a flat soap film can be bent into a hemisphere without having to fold. Furthermore interfacial tension of a soap film is not determined by external forces. When applying a point force to a system like the one described above with two rings spanning a soap film, the equilibrium state will be a very shallow catenoid. This does not have any resemblance to a tether, but it does look like the junction region between the tether and vesicle in figure 4.2.

Lipid bilayers resist bending, like macroscopic shells, but like soap films, they are fluid and have no geometric rigidity. This interplay between fluid and solid properties forms the basis for tether formation. To investigate tether formation further with respect to the model by Powers, consider the catenoid with a reservoir of lipid at a constant

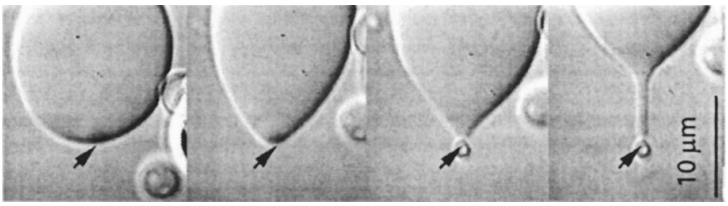

Figure 4.2: Equilibrium shapes of a vesicle subject to a point force exerted by optical tweezers [25].

chemical potential, μ, in figure 4.1 again. The surface tension $\phi = \mu/a$ is assumed to be much larger than the bending elasticity κ. By using the definition $\epsilon = \frac{\kappa}{\phi}$, the assumption can be written as $\epsilon \ll 1$. This situation corresponds to a tether experiment by Evans and Yeung [26] where a vesicle is aspirated into a pipette and a tether is pulled from it (fig. 4.3).

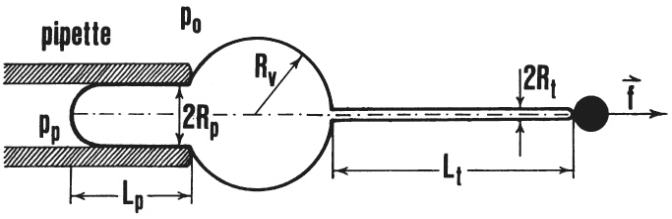

Figure 4.3: A vesicle is aspirated in a pipette and a tether is pulled with constant force (f) in the opposite direction. R_p is the pipette radius, L_t is the tether length, R_t is the tether radius, L_p is the pipette projection length, and R_v is the vesicle radius. The pressure surrounding the vesicle is p_0 and the pressure in the pipette is p_p [27].

The pipet suction decides the value of the tension, ϕ, and the part of the vesicle residing inside the pipette constitutes the lipid reservoir. The curvature of the vesicle is very small compared to the curvature of the tether, and the vesicle can therefore be considered as flat. When the surface tension is much larger than the bending elasticity as assumed above, there will be an elastic boundary layer near the small ring in figure 4.1 [24]. As h_0 increases, the amplitude of the catenoid increases until h_0 is in the order of $\sqrt{\epsilon}$ [24]. The amplitude of the catenoid cannot increase beyond this value. Instead the elastic boundary layer around the upper ring deforms into a thin cylinder for higher values of h_0 and a tether is formed. By taking the radius of the smallest circle to zero, $r_0 \to 0$, a point force can be modelled and the situation resembles pulling a tether from a cell by means of optical tweezers. Figure 4.4 shows the membrane shape for various ring separations.

The conclusion to the model is that the shape of a membrane subject to a point force

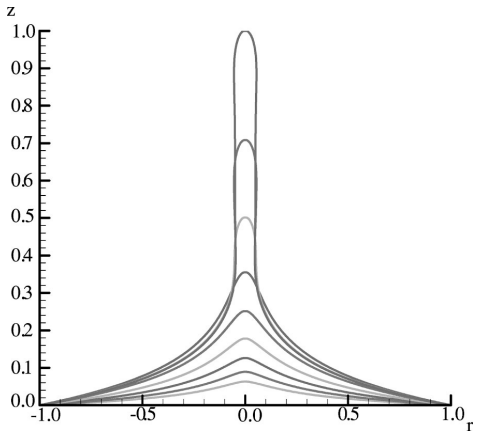

Figure 4.4: Membrane shape for various ring separations. $\epsilon = 0.005$ and $r_0 = 0.005$ [24].

and under high tension is best described as a boundary layer problem. The curves depicted in figure 4.4 stem from a numerical solution to the equations occurring from the boundary layer description, and so does the force-displacement curve in figure 4.5.

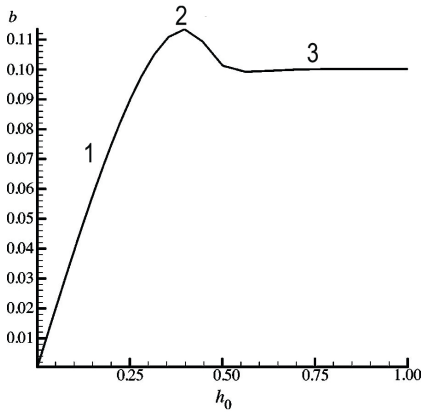

Figure 4.5: Axial force, b, as a function of displacement, h_0. The dimensionless curve results from the numerical solution to the model by Powers *et al.* with $\epsilon = 0.005$ and $r_0 = 0.005$. Modified from [24].

The force increases while the membrane deforms, corresponding to 1 in figure 4.5, and reaches a maximum value where the tether is formed, corresponding to 2 in figure 4.5. Then the force decreases slightly before reaching a constant value independent on the tether length, corresponding to 3 in figure 4.5.

This behaviour is also seen in experiments with giant vesicles. The two figures below show how tube formation deforms a vesicle (fig. 4.6(a)), and how the force develops over

time (fig. 4.6(b)). The maximum force, corresponding to the force where the vesicle deformation results in a tether, is called the overshoot force.

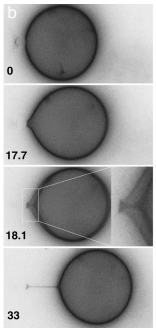

(a) Tube formation from a vesicle.

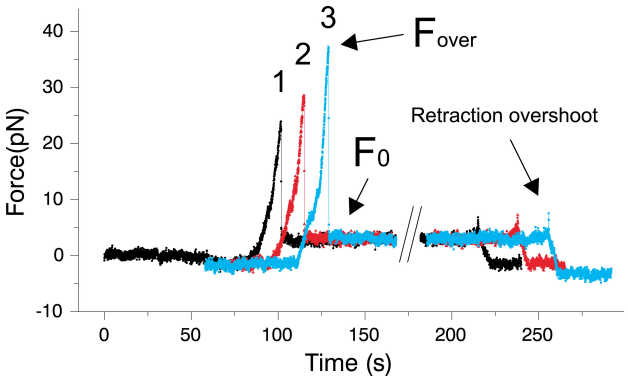

(b) Overshoot force. The three curves correspond to subsequent tube pulls from the same vesicle. After each pull the tether is retracted, and the tube is allowed to make further attachments to the bead.

Figure 4.6: The curves in b) show how the force develops with time when pulling a tether like in a). The overshoot force in b) corresponds to the force where the vesicle deformation in a) results in a tether. Pictures from [28].

4.2 Eukaryotic Tethers

Tethers extracted from eukaryotic cells are cylinders of phospholipid bilayers. Tethers have been pulled from eukaryotic cells such as outer hair cells [29], chick embryo fibroblasts and 3T3 mouse fibroblasts [30], neuronal growth cones [31], red blood cells [32], and neutrophils [33], [34], and the tether diameter has been observed to be smaller than 10 nm (pulled from red blood cells [35]), or larger than 100 nm (pulled form neuronal growth cones [31]).

Figure 4.7 shows a force-extension curve for a tether pulled from a fibroblast with optical tweezers. The curve has three regions. The first region is the initial phase where the tether is formed. Then there is an increase in force when the first micron of the tether is pulled out. This increase is linear, indicating that the tether has an elastic character. The second region is called the elongation phase. The force in this phase does not increase as the tether length is increased. This means that tether elongation does not depend on membrane stretching. In other words, there must be a membrane reservoir providing membrane material to the tether [30], indicating that the tether also has some viscous properties. The last region is the exponential phase where the reservoir apparently is drained and force is needed to deform the cell to make the tether longer. When looking

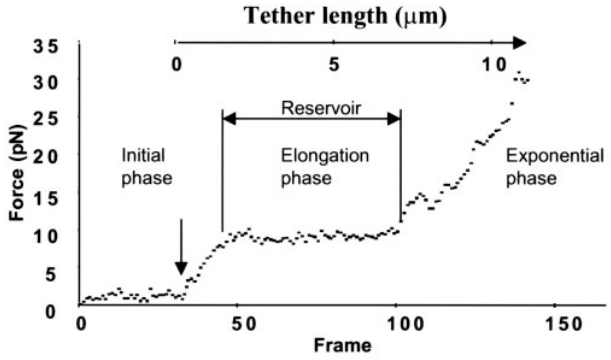

Figure 4.7: Force-extension relation for chick embryo fibroblasts and T3T mouse fibroblasts [30].

closer at the transition between the first and the second phase, it is possible to distinguish a force overshoot similar to that in figure 4.6(b). Overshoot forces are also observed in experiments with outer hair cells [29], and human embryonic kidney cells [36].

Several factors are seen to influence the forces involved in tether formation, and in the following I will describe some of these.

Tether force

The force needed to extract a tether from an eukaryotic cell has to overcome several barriers such as the bending rigidity of the membrane, the viscous resistance in the two monolayers forming the bilayer, and the adhesion of the bilayer to the cytoskeleton.

The bending energy is increased when pulling a tether because the cell body can be considered a plane with no curvature and membrane material from this disk is moved to the tether with a constant curvature. The viscous resistance in the bilayer stems from the membrane surface viscosity, η_m, the slip viscosity between the two monolayers, η_{si}, and the slip viscosity between the membrane and the cytoskeleton, η_{sc} (fig. 4.8).

Several experiments show that when the cytoskeleton in a cell is destroyed, the force required to pull a tether is decreased considerably [30], [33], [38]. This means that a large part of the tether force is used to separate the bilayer from the cytoskeleton.

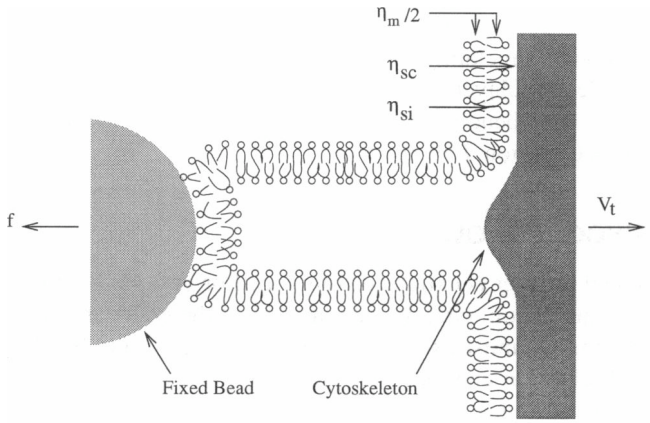

Figure 4.8: Schematic drawing of a tether being pulled off a cytoskeleton at the velocity V_t [37]. The force f is created by an optical laser trap. η_m is the membrane surface viscosity, η_{si} is the slip viscosity between the two monolayers, and η_{sc} is the slip viscosity between the membrane and the cytoskeleton.

Attachment area

Figure 4.6(b) showed three consecutive pulls from a giant vesicle of the same tether attached to a bead. After each pull, the tether was retracted and allowed to make further attachments to the bead. This increased the area of attachment, as seen in figure 4.9, and it has been shown that the tether force increases linearly with the area [28].

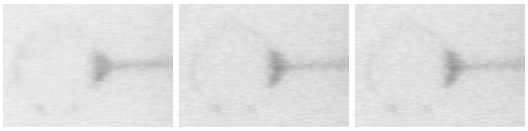

Figure 4.9: Inverted contrast fluorescence images showing that the attachment area between the bead and the membrane tube increases after subsequent tube pulls [28].

Velocity

The force needed to pull a tether is also seen to depend on the pulling speed. Figure 4.10 shows that the force increases when the pulling velocity is increased. This can be ex-

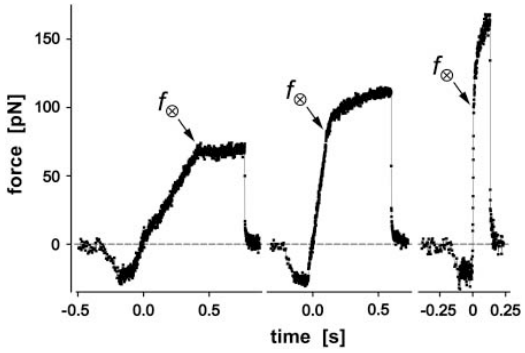

Figure 4.10: Force-time curves for P-selectin:neutrophil attachments at three different pulling speeds (2, 15 and 50 μm/s) [39]. The force $f_\otimes$ corresponds to the termination of the initial elastic regime and the onset of the tether flow regime corresponding to the elongation phase in figure 4.7.

plained by the fact that for higher pull velocities, the membrane material has less time to flow into the tube, and thus the force required to pull a tether is higher. In accordance with this, low pull velocities lead to increased tether length before the tether breaks [30].

Relaxation

Another feature of tethers is their viscous properties mentioned in the beginning of this section regarding figure 4.7. Zero-velocity measurements where a tether is held at a constant length show that the force holding the tether obeys a Maxwell-like exponential relaxation (fig. 4.11).

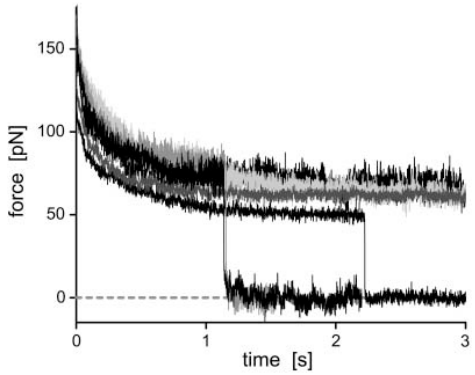

Figure 4.11: Zero-velocity measurements of 6 tethers from white blood cells [39]. The sudden jumps in force for two of the curves correspond to the tethers breaking. The force-time relation is Maxwell-like.

The Maxwell model (fig. 4.12) is represented by a purely elastic spring, corresponding to the tether, connected to a purely viscous damper, corresponding to the membrane.

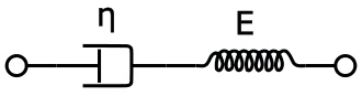

Figure 4.12: Illustration of the Maxwell model. A purely elastic spring with spring constant E is connected to a purely viscous damper with viscosity η [*http://en.wikipedia.org/?title=Viscoelastic*].

When the membrane material is put under a constant stress, the strain will have two components. The first is an elastic component which occurs immediately after stress is applied and relaxes immediately after the stress is released. The second component is viscous and increases with time as long as the stress is applied. The Maxwell model states that the stress applied decays exponentially with time obeying the relation

$$F \propto \exp\left(\frac{-(t - t_0)}{\tau}\right). \tag{4.2.1}$$

Here t is the time, t_0 is the initial time, and τ is the characteristic time for the relaxation. The relaxation time is a measure of the time required for the energy stored in the spring (the tether) to shift to the dash-pot (the membrane) and dissipate. Zero-velocity measurements then result from the viscous properties of the membrane.

4.3 Bacterial Tethers

In [40], L. Jauffred proposes a model for elastic bacterial tethers. This model suggests that the prokaryotic tethers pulled from *E. coli* bacteria resemble the eukaryotic tethers described above in that they are visco-elastic and composed of the outer membrane of the bacterium. This part of the membrane is a bilayer consisting of an outer leaflet of LPS and an inner leaflet of phospholipids as described in chapter 2 (fig. 4.13).

By adding different enzymes attacking specific parts of the *E. coli* membrane and considering how they influence the ability of pulling tethers, the model has been verified [40].

Tethers can only be pulled from smooth and rough strains of *E. coli*, while deep rough chemotypes missing both the O-antigen and the outer core of LPS do not have the ability to form tethers [40]. Furthermore, it has not been possible to extract tethers from Gram-positive *Bacterius Subtilus* [23] which have no LPS leaflet. This also supports the model

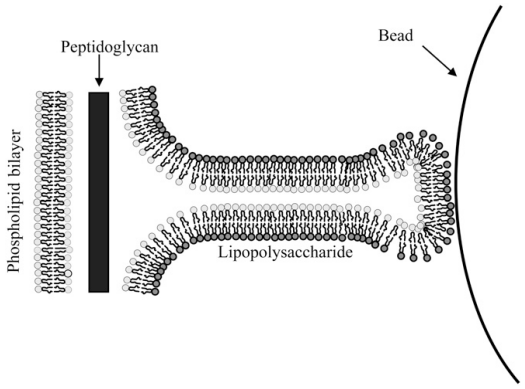

Figure 4.13: Proposed model of a visco-elastic bacterial tether from a rough bacterial strain. The tether is assumed to consist of the LPS and phospholipid bilayer but not of the peptidoglycan layer [40].

that tethers mainly consist of outer membrane material.

In contrast to experiments with eukaryotic tethers, no force overshoot is observed when pulling tethers from *E. coli* bacteria [40]. This is due to the fact that there is no cytoskeleton to separate from, and that the membrane immediately lets go of the peptidoglycan layer. Furthermore, the bacterial tethers do not experience an elongation phase where the force reaches a plateau, but have a linear force-extension relation. The spring constant for the bacterial tethers is found to be (11.6 ± 3.5) pN/μm for first pull tethers, i.e. tethers extended for the first time [40]. In comparison, the tether stiffness for the eukaryotic outer hair cells is 3.71-4.57 pN/μm [29], and the tether stiffness for human neutrophils and red blood cells is estimated to 130 pN/μm and 75-105 pN/μm, respectively [41].

The spring constant was shown to decrease with the number of consecutive pulls [23]. The final value reached in [23] was (5.7 ± 1.2) pN/μm. This supports the theory that the bacterial tethers are visco-elastic, as an irreversible relaxation takes place when pulling the same tether several times.

Furthermore, a Maxwell-like relaxation was also observed similar to that shown in figure 4.11 with a characteristic time τ = 207 s.

Chapter 5

Optical Tweezers

This chapter is devoted to a description of the theory behind optical trapping of particles. First, I will introduce optical tweezers (OT) as an instrument for trapping. Then I will describe how high precision position detection of trapped objects is achieved, and finally I will explain how the position detection can be used for force measurements by calibration.

5.1 Introduction to Optical Tweezers

The idea behind optical trapping was developed by Arthur Ashkin. In 1970 he published an article showing how radiation pressure could be used to accelerate and trap micron-sized dielectric particles [42]. In this first article about optical trapping, a single laser beam was demonstrated to accelerate a latex sphere in the direction of light propagation, while the sphere at the same time was drawn towards the centre of the beam (fig. 5.1(a)). By using two counter-propagating beams, the forward motion of a particle could be halted, and the particle was trapped (fig. 5.1(b)).

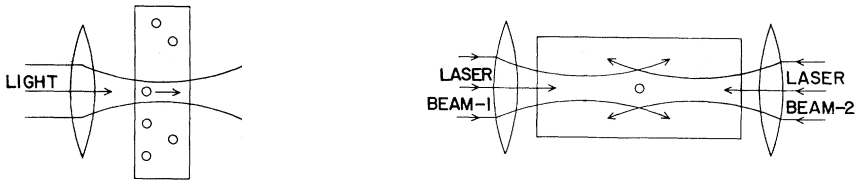

(a) First setup (b) Second setup

Figure 5.1: Schematic drawings of the first setups made by Ashkin. Laser light focused by a lens is used to manipulate a particle in a sample chamber. Pictures modified from [42]

In 1986, Ashkin *et al.* showed that particles could also be trapped with just a single

laser beam [43], a very great improvement to the method. By focusing the laser beam very tightly, the dielectric sphere could be trapped in the focal point, eliminating the need for a second, counter-propagating laser beam. This setup was called optical tweezers.

5.2 Optical Trapping Theory

Optical trapping of an object can be seen as the result of several optical forces, but the common fundament for these forces is the momentum carried by light. Each photon in a laser beam carries the momentum

$$p = \frac{E}{c} = h\lambda, \tag{5.2.1}$$

where $E = h\nu$ is the energy of a light quantum with frequency ν and wavelength λ, c is the speed of light, and h is Planck's constant. When the photons from a laser beam interact with a particle, a transfer of momentum may occur, and the particle senses a radiation pressure. Under normal conditions, radiation pressure from a light source is by no means strong enough to influence macroscopic objects. We do, for example, not feel any momentum transfer from the sun light. If the laser intensity is high and the beam is tightly focused, however, optical forces become significant on microscopic objects. The force arising from the momentum transfer can be written

$$F = Q\frac{nP}{c}, \tag{5.2.2}$$

where Q is a dimensionless efficiency factor, n is the refractive index of the medium, P is the power of the laser beam, and c is the velocity of light.

Some general conditions must be fulfilled for a particle to be trapped. The particle must be dielectric and transparent to the laser light, and it must have a refractive index higher than that of the surrounding medium due to reasons I will explain in the next sections. Furthermore, optimal trapping is achieved for spherical objects, as their curved surface resemble lenses diffracting the light.

A theoretical description of the optical trapping forces depends on the size of the object compared to the wavelength of the laser light. If the diameter of the sphere is much larger than the wavelength of the light, $d \gg \lambda$, basic ray optics can be used to describe the resulting forces. This case is called the Mie regime. If the diameter of the particle is much smaller than the wavelength of the light, $d \ll \lambda$, the sphere can be considered a point dipole. In this case, the Rayleigh regime, an electromagnetic approach is appropriate. The case where $d \approx \lambda$ is much more complicated, but as the experiments

in this thesis are carried out in that regime, it will be described briefly.

5.2.1 Ray optics or Mie regime

In the Mie regime, basic ray optics is sufficient to describe optical trapping. In this approach, the incoming laser beam can be decomposed into individual rays propagating in straight lines in media with the same refractive index [44]. Each ray can change direction due to refraction and reflection and changes polarisation at dielectric interfaces according to the Fresnel equations. Diffraction effects are per definition neglected in this limit. The laser beam must have an intensity profile with a strong gradient in order to trap a particle. One type of intensity profile fulfilling this requirement is the Gaussian, in which the light intensity is strongest in the middle of the beam and decays toward the edges. A laser with a Gaussian intensity profile is said to be operating in TEM_{00}-mode[1], which implicates that it has no electric or magnetic field in the direction of propagation. All beams mentioned in this thesis will be assumed to have a Gaussian intensity profile.

In the Mie regime, the trapping forces arise solely from momentum transfer. Consider a dielectric, spherical object with a refractive index, n_b, higher than that of the surrounding medium, n_m, for example a polystyrene bead in water ($1.59 > 1.33$). When the laser light hits the bead, it will change direction due to the difference in refractive indexes between the bead and the medium in accordance with Snell's law

$$n_m \sin\theta_m = n_b \sin\theta_b, \tag{5.2.3}$$

where θ_m is the incidence angle of the light and θ_b is the transmission angle. This change in direction of course also leads to a change in the momentum of the light, and due to the law of momentum conservation, the particle will experience an equal and opposite change in momentum. The resulting force on the bead will be perpendicular to the light's path in the bead and point away from the centre (fig. 5.2). Due to the higher refractive index of the bead, it will act as a focusing lens for the laser light. Furthermore, due to the Gaussian intensity profile of the beam, the momentum transfer from the rays in the middle of the beam will be larger than the momentum transfer from the edge rays. As a result, the net force will pull the bead toward the optical axis, as sketched in figure 5.2.

If the sphere would have a refractive index lower than that for the surrounding medium, it would be pushed out of the trap. This has been shown by Ashkin for air bubbles in glycerol [42].

The net force on the sphere can be split into two components [45], described by F_z and

[1] TEM stands for Transverse ElectroMagnetic

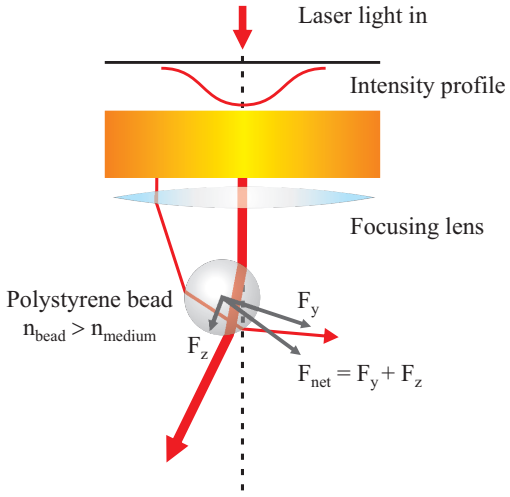

Figure 5.2: Schematic drawing of the ray optics model for optical trapping. Red arrows symbolise the light path for two representative rays, and grey arrows symbolise the momentum transferred to the sphere. The thickness of the arrows is proportional to the light intensity. Figure kindly provided by Andreas Blicher.

F_y, where F_z points in the direction of light propagation and corresponds to a scattering force, and F_y points in the direction of the light gradient and corresponds to a gradient force [46].

$$F_z = \frac{n_m P}{c}\left\{1 + R\cos 2\theta - \frac{T^2[\cos(2\theta - 2r) + R\cos 2\theta]}{1 + R^2 + 2R\cos 2r}\right\} \tag{5.2.4}$$

$$F_y = \frac{n_m P}{c}\left\{R\sin 2\theta - \frac{T^2[\sin(2\theta - 2r) + R\sin 2\theta]}{1 + R^2 + 2R\cos 2r}\right\} \tag{5.2.5}$$

The factor $\frac{n_m P}{c}$ is the incident momentum per second from eq. 5.2.2, and T and R are the Fresnel transmission and reflection coefficients. T and R are functions of the polarisation of the incoming light, and therefore the forces are polarisation dependent. θ and r correspond to the incidence and refraction angles, respectively. Since the formulas sum over all scattered rays, they are exact.

If the bead is above the focal point of the laser beam, as in figure 5.2, the net momentum will point downwards and a restoring force will pull the bead into the focus. Likewise, if the bead is below the focal point, the net momentum will point upwards and the bead is again pulled into the focus.

5.2.2 Rayleigh regime

For $d \ll \lambda$, the ray optical approach does not give a satisfying explanation of the forces acting on the sphere. In the Rayleigh regime the laser beam can be described by an electromagnetic wave, which induces electric dipoles in the dielectric sphere. Since $d \ll \lambda$, the sphere can be regarded as a point dipole. Near the focal point, the electric field of the laser is very non-uniform, and the dipole will therefore be affected differently at each monopole. This makes the sphere sense a net force in the direction of the intensity gradient. Furthermore, the dipole will absorb and reemit the incoming light leading to a momentum transfer. Consequently, the net force acting on the sphere can, as in the ray optics regime, be split into two components: A gradient force F_{grad} and a scattering force F_{scat}. The gradient force is in [43] given as

$$F_{grad} = \frac{1}{2} n_m^2 \alpha \times \nabla \left\langle E^2 \right\rangle, \tag{5.2.6}$$

where $\left\langle E^2 \right\rangle$ is the mean square electric field and α is the polarisability of the sphere given by

$$\alpha = r^3 \left(\frac{m^2 - 1}{m^2 + 2} \right), \tag{5.2.7}$$

where m is the effective refractive index $\frac{n_b}{n_m}$.

The scattering force can be described by

$$F_{scat} = n_m \frac{\sigma \langle S \rangle}{c}, \tag{5.2.8}$$

where $\sigma = \frac{8}{3}\pi k^4 r^6 (\frac{m^2-1}{m^2+2})$ is the scattering cross-section of the particle. $k = 2\pi n_m/\lambda$ is the wave number of the light, and $\langle S \rangle$ is the Poynting vector representing the energy flux of the electromagnetic field [47].

For the trap to be stable in the axial direction, the backward axial gradient force must balance the forward-scattering force. This condition can be fulfilled by tightly focusing the laser beam and in that way increasing the intensity gradient. The balancing of the two forces leads to a displacement of the equilibrium point for the particle so that it is located slightly below the focal point.

The two regimes described above can be used to gain an intuitive understanding of the forces in play when trapping. They do not, however, give a description of the middle regime where $d \approx \lambda$.

The conditions I have been working under fall in exactly this regime, with $\lambda = 1064$ nm and $d = 1010$ nm due to reasons discussed in section 6.1. A theoretical description of the middle region is quite complicated, but the next section gives a short overview.

5.2.3 Middle regime

In [48], Rohrbach has made a theoretical description of the regime in between the Mie and the Rayleigh regimes. Like the Rayleigh theory, this model uses a two-component approach dividing the force into a gradient component and a scattering component.

First the total scattered field is obtained with Mie theory, and then the trapping forces are found from the Lorentz force density for dipoles, finally giving the expression

$$\begin{aligned} \mathbf{F(b)} &= \mathbf{F_{grad}(b)} + \mathbf{F_{sca}(b)} \\ &\approx \frac{\alpha_0 n_m}{2cV} \int_{V(b)} \Delta I_0(\mathbf{r}) d^3 r \\ &+ \frac{n_m}{kc} I_0(\mathbf{b})[C_{ext}(\mathbf{b}) \langle \mathbf{k_i(b)} \rangle - C_{sca}(\mathbf{b}) \langle \mathbf{k_s(b)} \rangle]. \end{aligned} \tag{5.2.9}$$

The particle position relative to the centre of focus is given by $\mathbf{b}$, α_0 is the polarisability on a volume element V, n_m is the refractive index of the surrounding medium, and c is the velocity of light. The incident intensity is denoted by I_0, k is the wave number, and $C_{ext} = C_{sca} = Q_{sca}\pi\frac{d}{2}^2$ corresponds to the cross sections of the extinction and redistribution of momentum. For a full derivation of eq. 5.2.9 see [48].

5.2.4 Trap properties

As mentioned, the focus must be very tightly focused in order for the trap to be stable. This is achieved with an objective lens of high numerical aperture (NA)

$$NA = n \sin\theta, \tag{5.2.10}$$

where n is the refractive index of the medium in which the lens is operating, and θ is the half of the maximum cone angle. The maximum cone angle is the angle of the light cone after the beam has passed the objective (fig. 5.3).

From eq. 5.2.10 it is seen that the numerical aperture is high when the convergence angle θ is high. In this case, wide-angle rays important for the gradient force will be present. Ashkin [46] examined how θ affects the efficiency parameter Q from eq. 5.2.2. In [46] it is shown that for a polystyrene bead in water with an effective refractive index $n = \frac{1.59}{1.33} \approx 1.2$, a maximum efficiency parameter Q is achieved for $\theta \simeq 70°$. In order to

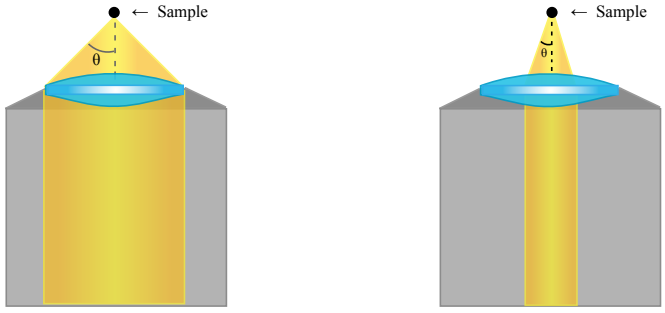

(a) Filled objective (b) Underfilled objective

Figure 5.3: Illustration of the maximum cone angle θ for: a) A slightly overfilled objective and b) an underfilled objective.

get the contribution from the extreme rays and thereby increase the ratio of trapping to scattering force, it is necessary to fill the objective [46] (fig. 5.3). This is done by inserting a beam expander in the laser path that can assure that the beam width is equivalent to the diameter of objective lens. Eq. 5.2.10 furthermore shows that the numerical aperture can be increased by using a medium with high refractive index, e.g. water ($n = 1.33$) or immersion oil ($n = 1.518$).

The problem with using immersion oil is that the difference in refractive index for the oil and the sample medium increases spherical aberration which in turn decreases the trap strength. Spherical aberration is a phenomenon occurring when light rays passing through a lens do not reach the same focal point (fig. 5.4), and they increase with trapping depth.

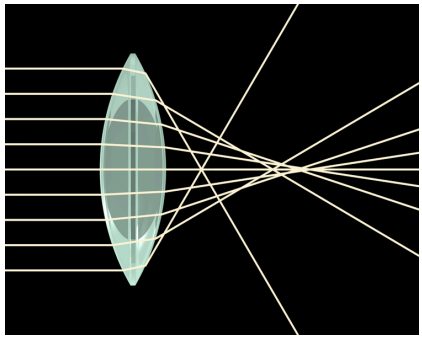

Figure 5.4: Spherical aberration is a phenomenon where parallel light rays passing through a lens are not focused in the same point. This effect becomes more pronounced when there is a change in refractive index after the rays have passed the lens. Figure from [*http://da.wikipedia.org/wiki/Sfærisk_aberration*].

Reihani and Oddershede have shown that the trap strength for a 1.01 μm polystyrene

bead 6 μm above the surface is only half of the trap strength at 3 μm when using an immersion oil with n = 1.518 [49], and at 10 μm the trap strength is almost zero. This means that trapping in a sample should be done as close to the bottom cover-slide of the sample chamber as possible in order to decrease the resolution and the axial optical trapping strength.
In addition to increasing the trapping strength, a high NA also results in a higher resolution of the sample when used as a microscope objective. The size of the finest details that can be imaged is namely λ/NA, where λ is the wavelength of the laser. Furthermore, a lens with a high numerical aperture will collect more light and will therefore give a brighter image.

5.3 Position Detection

In order to be able to do precise force measurements with the optical tweezers, it is necessary to know exactly where the bead is positioned compared to the centre of the trap.

Position detection is done by a quadrant photodiode (QPD) consisting of four separate photodiodes numbered from the upper left corner to the lower left corner as depicted in figure 5.5. The QPD receives its signal from the condenser collecting both scattered light from the trapped bead and non-scattered light from the laser (fig. 5.5).

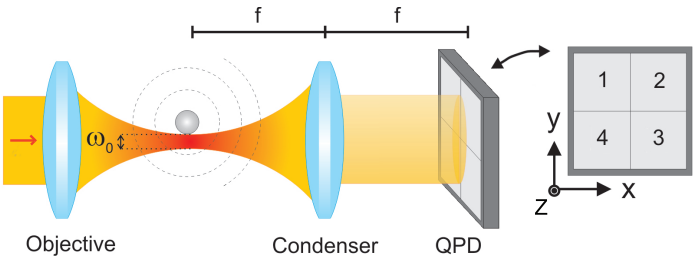

Figure 5.5: Schematic drawing of a bead trapped with optical tweezers. ω_0 is the width of the beam waist, and f is the focal length. Modified figure from [50].

The distribution of the incoming light induces a voltage difference over the QPD proportional to the intensity of the light. This voltage read-out can then be transformed into a displacement distance. The function of the photodiode will be explained below, while the conversion from voltage to distance will be described in section 5.4.

5.3.1 Quadrant photodiode

Each of the four diodes in the QPD is a Si PIN structure consisting of three silicon layers, namely a P-type semiconductor region, an Intrinsic semiconductor region, and an N-type semiconductor region (fig. 5.6).

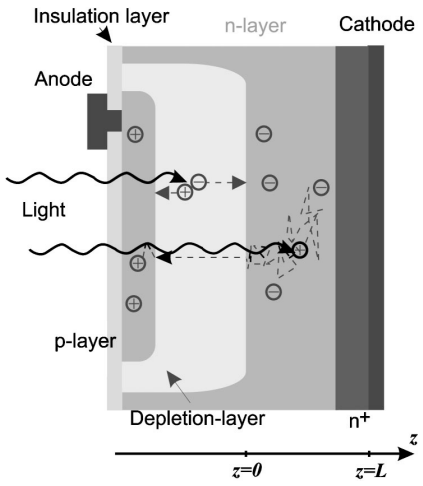

Figure 5.6: Cross section of a PIN photodiode seen from the side [51].

The intrinsic layer, corresponding to the depletion layer in figure 5.6, is a wide, lightly doped region, while the p- and n-layers are heavily doped. When light hits the diode, photons are absorbed in the silicon layers. This leads to excitation of valence electrons into the conduction band, whereby electron-hole pairs, also called carriers, are created. When the absorption happens in the depletion layer, the electric field originating from the charges in the p-layer and the n-layer causes the carriers to be separated within nanoseconds. The holes travel towards the anode through the p-layer and the electrons travel towards the cathode through the n-layer, thereby creating a photocurrent.

At infrared wavelengths, however, the photodiodes do not work quite as intended. The absorption coefficient for silicon is small for wavelengths within this region[2], making the diodes effectively transparent. This means that electron-hole pairs are created throughout the diode and not only in the intrinsic layer as intended [51]. The p-layer is so thin that the contribution from it can be neglected, but the carriers created in the n-region will give rise to a current additional to the response from the intrinsic region. This current is delayed with respect to its cause. This is because both the n-layer and the p-layer are field free, and consequently electrons and holes created in these areas will only move by

[2] less than 1 cm^{-1} at 300 K

thermal diffusion. It therefore takes up to several microseconds before the carriers reach the depletion region and are pulled across it by the electrical field. As described in [51], the additional slower reaction for high frequencies makes the photodiode act as a low pass filter of first order with the characteristic function

$$\frac{P(f)}{P_0(f)} = \frac{1}{1 + (f/f_{3dB})^2}. \tag{5.3.1}$$

$P_0(f)$ is the absolute square Fourier transform of the input signal, and $P(f)$ is the absolute square Fourier transform of the output signal. For the photodiode used in the OT laboratory, we have $f_{3dB} \approx 8$ kHz. The unintended filtering of the position signal leads to an apparent increase in the trap stiffness, and this must be accounted for through calibration, if very accurate position measurements are desired.

5.3.2 Photodiode response

The voltage difference over the QPD is proportional to the intensity of the incoming light, and therefore the difference in light intensity between two halves of the photodiode can be calculated as follows:

$$V_x = \frac{(V_1 + V_4) - (V_2 + V_3)}{V_1 + V_2 + V_3 + V_4}$$

$$V_y = \frac{(V_1 + V_2) - (V_3 + V_4)}{V_1 + V_2 + V_3 + V_4}$$

V_x is then a dimensionless number corresponding to the intensity difference between the left and the right halves of the photodiode normalised by the total intensity, and V_y is the intensity difference between the upper and the lower halves normalised by the total intensity. This photodiode response to the intensity distribution has been shown to be linearly correlated with the position of the trapped sphere compared to the centre of the trap, if the displacement of the sphere is smaller than a few hundred nanometers [52] (fig. 5.7). That requirement is fulfilled in the experiments conducted in this thesis, and therefore V_x is proportional to the displacement of the sphere in the x-direction, and V_y is proportional to the y-displacement. The conversion factor, A, between the voltage signal and the physical displacement can be found by calibration.

5.4 Calibration

To be able to use the QPD for force measurements, two calibrations must be done. The first has already been mentioned above and is concerned with converting the voltage signals from the photodiode into physical displacement. The second is concerned with trans-

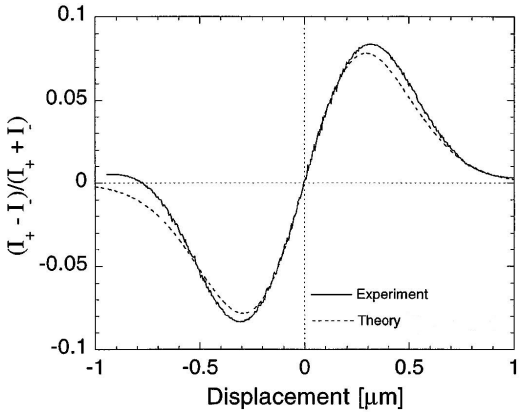

Figure 5.7: Figure from [52] showing that for small displacements the photodiode response to the intensity distribution is linearly correlated with the position of a trapped sphere.

lating the displacement into an applied force. This is done by finding the stiffness of the laser trap, κ_{trap}. When this is known, the force applied to the bead can be calculated by Hooke's law

$$F = -\kappa_{trap} x, \tag{5.4.1}$$

as the displacement x of the bead relative to the centre of the trap is known from the first calibration step.

The two conversion factors, A and κ_{trap}, can be found by considering the power spectrum of the position distribution of a bead in the trap due to Brownian motion. This method of calibrating is called the power spectral density analysis, and it will be discussed in more detail in section 5.4.2. Calibration can be done in several other ways, but I will only describe the method just mentioned, as it is the one used in the OT laboratory at the Niels Bohr Institute.

5.4.1 Brownian motion

A micron-sized object in a liquid solution will constantly be bombarded by other molecules leading to rapid chaotic movements of the particle. The energy transferred between the particles during collision is given by the equipartition theorem and equals $\frac{1}{2}k_B T$. The mean square displacement of a bead of radius r due to Brownian motion is in one dimension given by

$$\left\langle x^2 \right\rangle = 2Dt, \tag{5.4.2}$$

where t is the time elapsed since the particle started at $x = 0$, and D is the diffusion constant

$$D = \frac{k_B T}{6\pi\eta r}. \tag{5.4.3}$$

Here η is the viscosity of the liquid, k_B is the Boltzmann constant, T is the absolute temperature, and $\gamma = 6\pi\eta r$ is the Stokes drag constant.

When the bead is trapped with the optical tweezers, it experiences the trap as a harmonic potential, and the Brownian motion is restricted according to the strength of the trap. The potential of the harmonic oscillator in one dimension is

$$U(x) = \frac{1}{2}\kappa_x x^2, \tag{5.4.4}$$

where κ_x is the spring constant and x is the displacement.

The probability of finding the bead at a distance x from the starting point is for a Boltzmann distribution $P(x) = \frac{\exp(-k/k_B T)}{Z}$ in a harmonic potential given by

$$G(x) \propto \exp\left(\frac{-\kappa_x(x - \langle x\rangle)^2}{k_B T}\right). \tag{5.4.5}$$

Figure 5.8 shows the Brownian motion for a trapped bead as a function of time. Both axes have arbitrary units.

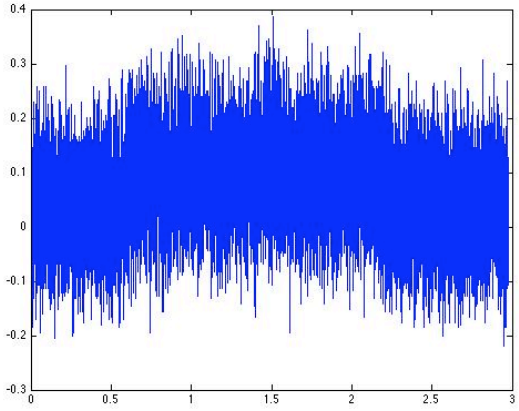

Figure 5.8: The Brownian motion in the x-direction for a trapped bead. Data from 07.05.08

5.4.2 Spectral analysis

The position distribution of a trapped bead is measured as a voltage signal from the QPD as described in section 5.3. The collected voltage measurements are a set of time-domain data. By Fourier transforming the data into a frequency-domain, a power spectrum is obtained. It is also possible to calculate a theoretical power spectrum for the Brownian motion, and by fitting the theoretical spectrum to the experimental, the conversion factors can be found.

Below, I will describe first how to calculate the power spectrum of the measured voltage series. Then I shall describe how the theoretical power spectrum can be obtained, and finally I will explain how the conversion factors can be found by comparing the two spectra.

Experimental power spectrum

The output data from the QPD contains N discrete data points x_n separated by a time step δt. The Fourier components of this data set is found by

$$X(f_m) = \sum_{n=1}^{N} x_n e^{2\pi i n m/N}, \tag{5.4.6}$$

where each $X(f_m)$ corresponds to the frequency $f_m = m\delta f, -N/2 \leq m \leq N/2$.

The power spectrum $S(f_m)$ is calculated from the square of the modulus of $X(f_m)$. To ensure that only positive frequencies occur, a so-called one-sided power spectrum is calculated as follows:

$$\begin{aligned} S(f_m) &= \frac{2}{N^2 \delta f}|X(f_m)|^2, \\ 0 < m &< \frac{N}{2}, \\ S(f_0 = 0) &= \frac{1}{N^2 \delta f}|X(0)|^2, \\ S(f_{N/2}) &= \frac{1}{N^2 \delta f}|X(f_{N/2})|^2. \end{aligned} \tag{5.4.7}$$

The highest frequency in the power spectrum is $f_{N/2}$, which is called the Nyquist frequency. The negative frequencies which are not included in the one-sided power spectrum do not provide any information not already found in the positive spectrum, and thus no information is lost when reducing the original N data points by half.

Through a few steps, a relationship between $S(f_m)$ and the deviation is found

$$\sum_{m=1}^{N/2} S(f_m)\delta f = \left\langle x^2 \right\rangle - \langle x \rangle^2 = \sigma(x)^2. \tag{5.4.8}$$

Theoretical power spectrum

A trapped spherical object has the following equation of motion for the position $x(t)$ in one dimension:

$$m\ddot{x} + \gamma\dot{x} + \kappa x = F(t). \tag{5.4.9}$$

m is the mass of the particle, γ is the drag coefficient, and κ is the spring constant of the trap. x is the distance of the particle from the trap centre, and $F(t)$ is a random thermal force arising from the bombardment of the particle by other molecules in the solution. The mean value of F is zero, as the thermal collisions have no preferred direction, and assuming that F is a white noise force its power spectrum is a constant

$$|F(f)|^2 = 4\gamma k_B T. \tag{5.4.10}$$

As the Reynolds number for a micrometer sized object in a fluid is $Re \sim 10^{-3}$, which is much smaller than 1, the viscous forces on the object are dominant over inertial forces. In this case where there is no acceleration, the flow is laminar, and the first term in equation 5.4.9 can be neglected. The equation of motion then simplifies to a Langevin equation

$$\gamma\dot{x} + \kappa x = F(t). \tag{5.4.11}$$

The power spectrum of the position fluctuations can be found from the Langevin equation 5.4.11 as described below.

The Fourier transform of $x(t)$ is defined as $X(f)$ and thus

$$x(t) = \int_{-\infty}^{\infty} X(f)e^{-2\pi i f t}df. \tag{5.4.12}$$

This expression for $x(t)$ is substituted into equation 5.4.11:

$$\gamma\left(\frac{d}{dt}\int_{-\infty}^{\infty} X(f)e^{-2\pi i f t}df\right) + \kappa_x \int_{-\infty}^{\infty} X(f)e^{-2\pi i f t}df = \int_{-\infty}^{\infty} F(f)e^{-2\pi i f t}df. \tag{5.4.13}$$

The differential operator does not have the same variable as the integrand. Therefore, it

can be moved under the integral.

$$\gamma \int_{-\infty}^{\infty} X(f) \frac{d}{dt} e^{-2\pi i f t} df + \kappa_x \int_{-\infty}^{\infty} X(f) e^{-2\pi i f t} df = \int_{-\infty}^{\infty} F(f) e^{-2\pi i f t} df \tag{5.4.14}$$

$$\int_{-\infty}^{\infty} (\kappa_x - 2\pi\gamma i f) X(f) e^{-2\pi i f t} df = \int_{-\infty}^{\infty} F(f) e^{-2\pi i f t} df \tag{5.4.15}$$

finally yielding the relationship

$$(\kappa_x - 2\pi\gamma i f) X(f) = F(f). \tag{5.4.16}$$

By taking the square modulus on both sides in eq. 5.4.16, it is found that the power spectrum of $x(t)$ is

$$|X(f)|^2 = \frac{|F(f)|^2}{4\pi^2\gamma^2(f_c^2 + f^2)}, \tag{5.4.17}$$

where the corner frequency f_c is defined as

$$f_c = \frac{\kappa_x}{2\pi\gamma}. \tag{5.4.18}$$

The corner frequency is the point dividing low frequency events and high frequency events. At high frequencies, i.e. short time-scales, the bead does not have sufficient time to move so far away from the centre of the trap that it can feel the potential well. In other words, the bead does not feel the trap restriction and behaves as if free when above f_c. At low frequencies, i.e. long time-scales, the bead can move further away, and it will therefore feel the restriction of the trap. The stronger the trap, the higher the corner frequency.

By inserting eq. 5.4.10 into eq. 5.4.17, the power spectrum of $x(t)$ can be written as

$$|X(f)|^2 = \frac{k_B T}{\pi^2\gamma(f_c^2 + f^2)} = \frac{D}{\pi^2(f_c^2 + f^2)} \tag{5.4.19}$$

with the diffusion constant D defined in eq. 5.4.3.

5.4.3 Conversion factors

Now two different versions of the same power spectrum for the motion of a trapped bead have been obtained. One originates from the voltage series of the particle movement measured from the QPD, and the other is a Lorentzian function derived theoretically from the Langevin equation of motion. By fitting the Lorentzian function to the experimental spectrum, the corner frequency can be found (fig. 5.9).

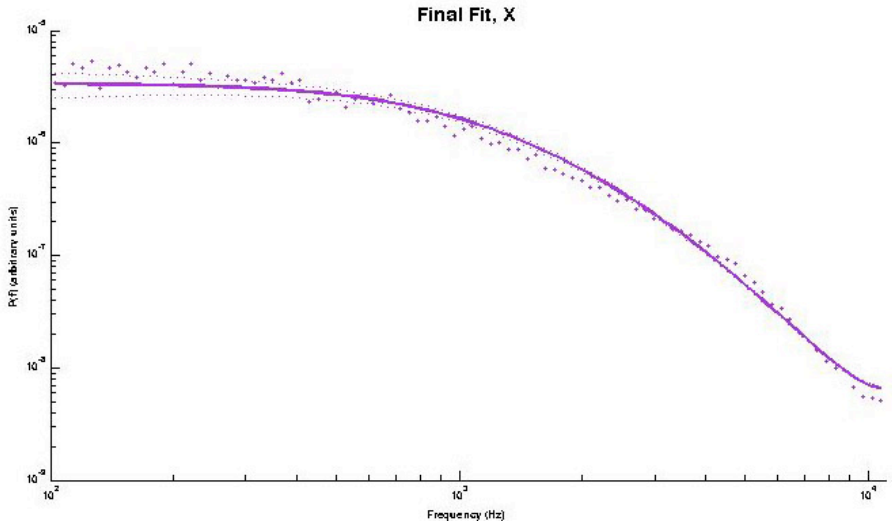

Figure 5.9: Power spectrum of the Brownian motion of a trapped bead. A Lorentzian function is fitted to the power spectrum and a corner frequency of (1218.7 ± 26.9) Hz is found. The power spectrum is created from the data shown in figure 5.8.

Since the value of γ for the bead can be calculated from $\gamma = 6\pi\eta r$, when the viscosity of the medium η is known, the spring constant for the trap can then be calculated as follows

$$\kappa_x = 2\pi\gamma f_c. \tag{5.4.20}$$

Thus one of the two conversion factors has been found. The fitting of the theoretical power spectrum is done with a Matlab program written by Hansen *et al.* [53]. It will be described in more detail in section 8.1.2.

The conversion factor A between voltage and distance is found by comparing the standard deviation σ_{V_x} of the measured x-positions with a theoretical value of the deviation σ_x. The theoretical value is found through the equipartition theorem stating that

$$\frac{1}{2}\kappa_x \left\langle x^2 \right\rangle = \frac{1}{2}k_B T. \tag{5.4.21}$$

The variance of the position distribution of a bead in the trap is given by $\sigma_x^2 = \left\langle x^2 \right\rangle - \langle x \rangle^2$, but the last term is zero because x is chosen as the deviation from the equilibrium position. Therefore, $\left\langle x^2 \right\rangle$ equals σ_x^2. By using this together with the fact that κ_x can be calculated from 5.4.20, σ_x can be found from 5.4.21.

The experimental value of σ_x is found by stacking the values V_x from the QPD corresponding to the x-position of the bead. The resulting histogram is fitted with a Gaussian,

and in this way a value for σ_{V_x} is found (fig. 5.10). This procedure is also conducted in the calibration program by Hansen *et al.* [53].

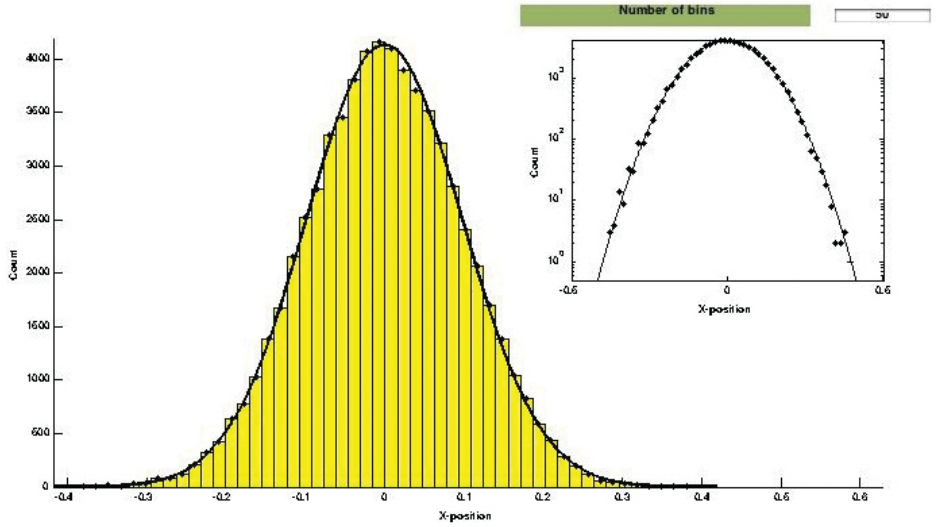

Figure 5.10: Histogram of the position of a trapped bead shown in figure 5.8. Here $\sigma_{V_x} = 0.98$. Data from 07.05.08.

Finally, the conversion factor A is found by

$$A = \frac{\sigma_x}{\sigma_{V_x}}. \tag{5.4.22}$$

To sum up, the force on a trapped bead can be calculated from the voltage output V_x from the QPD by

$$F_x = \kappa_x \cdot A \cdot V_x. \tag{5.4.23}$$

Chapter 6

Experimental Setup

This chapter describes how the experimental setup in the OT laboratory at the Niels Bohr Institute works.

6.1 Setup

The setup used for experiments consists of a commercial inverted light microscope [Leica, DM IRBE] with a build-in optical trap (fig. 6.1). The essential elements are a laser, a beam expander, a high NA objective, a movable sample holder, and a system to monitor the movement of trapped objects.

An inverted microscope functions exactly like a standard microscope, only is the condenser placed above the sample and the objective is placed below. Because the optical trap is build into the microscope, the objective, which is an oil objective with a high numerical aperture of 1.40, is used for both trapping and viewing. The sample is illuminated with a halogen lamp and can be observed in the microscope through the eyepieces as long as the laser is turned off. When the laser is on, the high intensity beam can cause permanent damage to the eyes, and the sample is therefore viewed with a CCD camera connected to a monitor and a VCR instead. To avoid eye-damage, security glasses should furthermore be worn. In order to ensure that the sample has the correct contrast without shadows or glare, the condenser is adjusted so that the focus of the light is in the same plane as the focus of the objective, a technique called Köhler illumination.

Laser light path

The laser used in the Optical Tweezers group at NBI is an Yttrium:Orthovanadate (Yt:VO_4) laser [Spectra Physics, Millennia IR] with a wavelength of 1064 nm. The laser output is

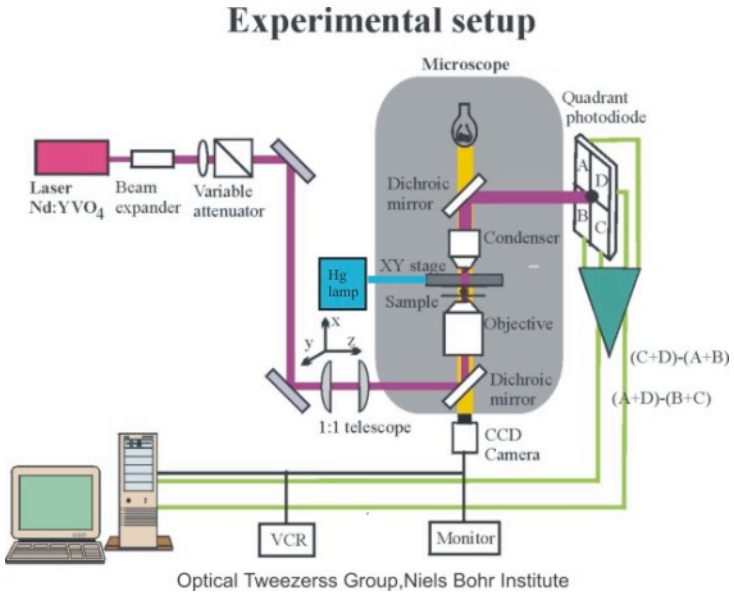

Figure 6.1: Experimental setup. Picture taken from [*http://www.nbi.dk/ tweezer/*].

less than 1 mm in diameter, but the beam is expanded to 8 mm and steered into the microscope, where it enters the objective. The back aperture of the objective is 7 mm, which means that it is slightly overfilled by the laser beam. The light then converges into a tightly focused diffraction limited spot which constitutes the optical trap as described in chapter 5. The light from the trapped particle is collected by a 1.4 NA oil condenser and projected onto a quadrant photodiode [S5981, Hamamatsu] by a dichroic mirror. By using a dichroic mirror, the light from the halogen lamp placed above the sample is allowed to pass through to the sample. The QPD is about 1x1 cm, and the beam incident on the photodiode is approximately 5 mm in diameter. For details on the light path, see [54].

The output from the QPD, which consists of four voltage signals from the four separate photodiodes corresponding to the position of the particle in the trap, are sent to a preamplifier, where it is transformed into two voltage signals V_x and V_y mentioned in section 5.3.2. The preamplifier has a build-in low-pass filter with a characteristic frequency $f_{3dB} = 80$ kHz. The signal from the preamplifier is passed on to an amplifier where gain and high-pass/low-pass filters can be adjusted to optimise the signal. The analogue signal from the amplifier can be viewed on an oscilloscope before it is converted into a digital signal which is recorded by a PC.

Piezo stage

The sample to be investigated is held in place with a sample holder, which is mounted on a piezo-electric stage. A piezo is a crystal that changes its shape when a voltage is applied to it, and it controls the motion of the sample relative to the microscope with a step size of 0.02 microns. The piezo stage itself is fastened to a stage which is less precise and is used for coarse position adjustment.

Measurements

When doing measurements, the lamp illuminating the sample is turned off as to minimise background noise. Then the diaphragm on the condenser is opened so that a maximal signal from the sample is passed on to the QPD. The laser beam must be centred on the QPD in order to assure that all experiments have the same off-set. Centring is done by adjusting the QPD vertically and horizontally using the signal on the oscilloscope as a guide.

Optical damage

When working with biological samples *in vivo*, it is important to use a wavelength not absorbed by the material in order not to harm living organisms. Wavelengths below 700 nm can be absorbed by proteins, and wavelengths above 1200 nm can be absorbed by water, so the transparent window in between these two limits is preferable. Figure 6.2 by Neuman *et al.* [55] shows that within this window, wavelengths between 850 nm and 950 nm are the most harming for *E. coli* bacteria, while wavelengths below 850 nm and above 950 nm are less damaging. The red arrow shows the wavelength of 1064 nm used for all experiments in this thesis. The sensitivity is given as a function of the rotation time for a flagella on a bacterium. LD_{50} is the half of the maximal rotation rate, and the sensitivity is defined as the reciprocal of LD_{50} [55]. The laser power employed in this thesis is around 100 mW in the specimen plane like in the Neuman experiment, but the laser is not directly incident on the bacteria.

Figure 6.2 only shows one way of measuring the damage on *E. coli* bacteria. When measuring other parameters such as expression of certain proteins or the pH gradient over the cell wall, a different result might be obtained. One experiment considering the pH gradient over the cell wall has been performed on *E. coli* by Rasmussen *et al.* [56] for a 1064 nm laser. *E. coli* bacteria were trapped with the laser for up to 60 minutes, and the intracellular pH was measured. The pH decreased to 50% of the initial value within 30 minutes for a laser power of 18 mW in the sample plane. As the experiments in the

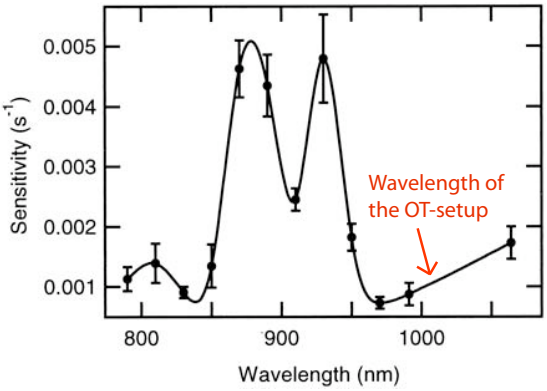

Figure 6.2: Action spectrum for *E. coli* trapped with a laser power of 100 mW determined in the specimen plane [55]. The laser beam is directly incident on the bacteria.

present thesis were run for no more than 400 seconds, and the laser beam as mentioned was not directly incident on the bacterium, the effect of the laser on the *E. coli* membrane is considered to be negligible. The extended tethers are also considered to be unaffected, as the beam width of the laser is approximately 1 μm, and the bead used as handle is either 1.01 or 1.26 μm in diameter.

Chapter 7

Experimental Procedure

In this chapter, I will describe how I have prepared samples for experiments, how the experiments were conducted and how data was acquired.

7.1 Sample preparation

The *E. coli* bacteria used in the experiments were a rough strain called SB. The particular mutant was a S2188 with the inserted plasmid pSB2267 [57] kindly provided by Stanley Brown, University of Copenhagen. The most important feature of the SB strain is that it cannot form pili.

Chambers containing bacteria and lectin-coated beads were prepared as described in appendix A.3. The beads used in this project were polystyrene beads with a diameter of either 1.01 μm or 1.26 μm and a refractive index of 1.59 (Bangs Laboratories, Inc.). Non-coated beads will adhere to *E. coli* due to non-specific binding, but to improve the specific interactions, the beads were coated with lectin, a protein which binds to carbohydrates and thereby also the LPS on the surface of *E. coli*. The coating procedure is described in appendix A.2.

The sample chambers were made of a large glass microscope slide of 24x50 mm, two pieces of double-layered, double-sided tape, and a small glass cover slip of 18x18 mm (fig. 7.1), and the final volume of the chamber was approximately 10 μL. When preparing samples with peptide, 10 μl peptide at a concentration of 2 μM were added just before sealing the chambers. For both arenicin-3 and novispirin, a concentration of 2 μM is above the MIC.

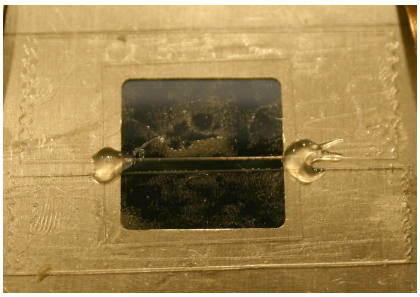

Figure 7.1: A perfusion chamber made of a large glass slide and a small glass cover slip separated by double-layered double-sided tape. The chamber ends are sealed with vacuum grease.

7.2 Data acquisition

Two different types of measurements have been performed in this thesis, namely force-extension measurements and relaxation measurements.

The force-extension measurements were carried out in order to find and compare the spring constant for membrane tethers both in the presence and absence of antimicrobial peptides. Relaxation measurements were carried out to be able to describe the physical properties of the tethers in more detail. As the force-extension measurements did not show any difference between the spring constants of tethers pulled with and without peptides present, the relaxation measurements were used to reveal further information.

All measurements were done 2 μm above the surface of the microscope slide in order to reduce interactions between the bead and the surface and to assure that the bead did not stick to any dirt on the microscope slide, thereby ruining the measurement. As the bacteria were adhered to the surface of the cover-slide, it was not possible to perform measurements deeper in the chamber. Furthermore, as explained in section 5.2.4, it was preferable to trap beads as close to the surface as possible when using an oil objective. When the distance between the bead and the surface is below approximately 5 μm, the Stoke's drag force is influenced by the surface, but this was taken into account when calibrating the measurements.

Both the force-extension measurements and the relaxation measurements were carried out by capturing a bead attached to a bacterium in the laser trap, moving the bead 2 μm away from the surface, and then moving the piezo stage 2 μm in the x-direction at constant speed. To assure that the distance between the bead and the surface was as constant as possible for the different measurements, the bead was brought into focus, and this position was set to zero on the microscope. Then, the turret holding the objective was adjusted and the position was read off the display on the microscope. Just after the

position reached '-2 μm', the turret was halted and the measurement was carried out. The piezo stage was controlled by the LabView program 'constantspeed1.vi' made by Nader Reihani. This program moved the stage in the x-direction with a constant speed and furthermore registered the output from the QPD. For each measurement, the desired speed and distance were entered in the programme along with the run time. The run time for a force-extension measurement where a tether was pulled 2 μm with 0.1 μm/s was consistently set to 21 seconds, giving a 1 second pause between stretching and unstretching. Relaxation measurements were made simply by extending the run time to 300 seconds.

'constantspeed1.vi' created two data files, one containing the data for stretching, i.e. moving the stage to the maximum displacement, and the other containing the data for unstretching, i.e. moving the stage back to the starting point. The files consist of three columns. The first contains the voltage signal in the x-direction from the QPD, V_x, the second contains the voltage signal in the y-direction, V_y, and the last contains the voltage signal from the piezo stage, V_{ps}. The output from the QPD was translated into a force as explained in section 5.4.3, and the voltage signal from the piezo stage was converted into a metric distance by a conversion factor characteristic for the piezo stage.

As mentioned in section 5.4.3, the conversion factors were found from the power spectrum of a free bead. The data of the motion used to create the power spectrum were also acquired with a LabView program, 'OnlineCalibration3.vi'. This program required only one input, namely the laser power. The output file contained three columns. The first contains the time and the last two contain the motion in the x- and the y-direction, respectively.

On the 14/5 we discovered that the channels for x and y on the amplifier had been interchanged meaning that the x-signal from the photodiode was recorded as y and the y-signal was recorded as x in the program I used. To make sure that the channels really were interchanged, a simple test was performed.

A chamber containing 1.26 μm beads was prepared and put into the microscope. The laser was turned on, and the empty trap was centred on the QPD using the screw knobs on the photodiode. Then a bead stuck to the surface of the microscope slide was captured in the trap, and the laser beam was again centred on the photodiode, this time using the stage. When the bead was placed directly in the middle of the laser beam, the stage was moved first in the x-direction and then in the y-direction. By observing which channel reacted on the oscilloscope when the stage was moved in the different directions, it was possible to determine that the two channels had been interchanged. The consequence of this is that the first column in the data file contains V_y instead of V_x while the second

column contains V_x instead of V_y for data recorded before 14/5. As both signals were recorded, no data was missing, and V_y was simply treated as V_x when doing the data analysis. A few corrections had to be made when converting the signals to force and extension, however. These will be mentioned in section 8.1.1.

The only serious consequence of the interchanged channels was that the immediate on-line coarse data analysis performed by 'constantspeed1.vi' was only made on the supposed x-signal. This analysis was used to judge if the measurement just performed could be used or not, and thus I chose which data to save and which to discard on a wrong basis. This was corrected in later measurements.

Chapter 8

Results and Discussion

The first part of this chapter describes how the data for both force-extension measurements, relaxation measurements, and calibration was analysed. The second part of the chapter presents the results I have obtained.

8.1 Data analysis

All data analysis was done with Matlab programs. The force-extension and relaxation measurements were analysed with programs written by L. Jauffred, and the calibration measurements were analysed with the program 'tweezercalib' written by Hansen *et al.* [53].

8.1.1 Force-extension and relaxation measurements

Analysis of the data was as mentioned done with MatLab programs written by L. Jauffred. The programs were modified to better suit the needs of my data analysis.

Force-extension

The MatLab program used for analysis of the force-extension measurements is called main.m, and it loaded the files for both stretching and for unstretching. More precisely, the column containing the voltage signal from the piezo and the column containing V_x from the QPD was loaded. For data before 14/5 the V_y column was loaded instead of the V_x column. After the files were loaded, a sliding window with a size of 12000 points was used to smooth the stretching data. This was done due to artificial oscillations occurring in some of the measurements which will be discussed in section 8.2.1. The unstretching data was not smoothened as only the stretching data was used when calculating the tether stiffness. After applying the sliding window, the data was further averaged by replacing

every 1000 data points with the mean of them so that the number of data points were reduced with a factor 1000. This was done to decrease the number of data points, which was otherwise quite big as the sampling frequency was 5 kHz and the experiments were recorded for 21 s. Then the corner frequency f_c and the standard deviation σ_{V_x} obtained from the calibration were used to calculate κ_x and the conversion factor A as shown in eq. 5.4.20 and eq. 5.4.22 in section 5.4.3, respectively. A gave the translation constant for voltage to metric units for the photodiode, and the voltage signal from the piezo stage was translated by the conversion factor $B = 10^{-5}$ m/V which, as mentioned earlier, does not depend on the measurements. Now it would be tempting to think that the distance on the x-axis could just be calculated by multiplying the movement of the piezo stage with B, but one more step was needed. Multiplying V_{ps} with the conversion factor B gives the distance from the bacterium to the centre of the trap, but the desired distance was that from the bacterium to the place on the bead where the tether was attached (fig. 8.1).

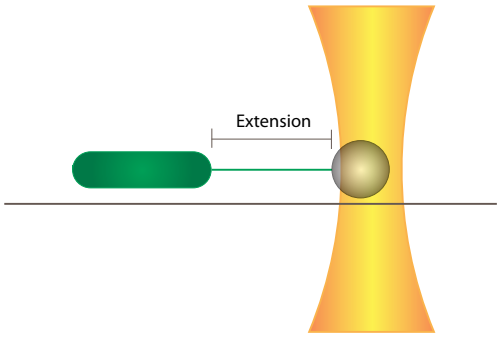

Figure 8.1: Tether extension. The tether length is the distance from the bacterium to the rim of the bead.

This extension was calculated by subtracting the radius of the bead and the displacement of the bead in the trap from the distance found from the data file. This was done under the assumption that the tether was attached to the bead at the point closest to the bacterium. Since the bead could freely rotate in the trap, this is a reasonable assumption. Thus the distance at each data point was calculated as follows:

$$x = B \cdot V_{ps} + A \cdot V_x - r - x_0. \tag{8.1.1}$$

The first term is the distance between the bacterium and the centre of the trap. The second term corresponds to the displacement of the bead in the trap. The second term was added to the first because the directions of the QPD and the piezoelectric stage were

oppositely defined. r is the radius of the bead, and x_0 is an arbitrary starting point. Since the extension is the relative distance between the bead and the bacterium, the starting point was set to zero by subtracting x_0.

The force was found by multiplying the V_x signal from the QPD with κ_x and A as given by eq. 5.4.23. Furthermore, the viscous drag on the bead was subtracted. It is given by Stoke's law $\gamma \cdot v$, where $\gamma = 6\pi\eta r$ is the Stoke's drag and v is the velocity of the fluid relative to the bead which equals the velocity of the stage. To sum up, the force on the bead due to the tether was found by

$$F = \kappa_x \cdot A \cdot V_x - \gamma \cdot v. \tag{8.1.2}$$

The last term is approximately hundred times smaller than the first term and thus does not contribute noticeably to the tether force.

Finally the force was plotted against the extension and the curves were fitted linearly (fig. 8.2). The slope of the fit corresponds to the spring constant of the tether, κ_t. In figure 8.2, $\kappa_t = 29.8$ pN/μm.

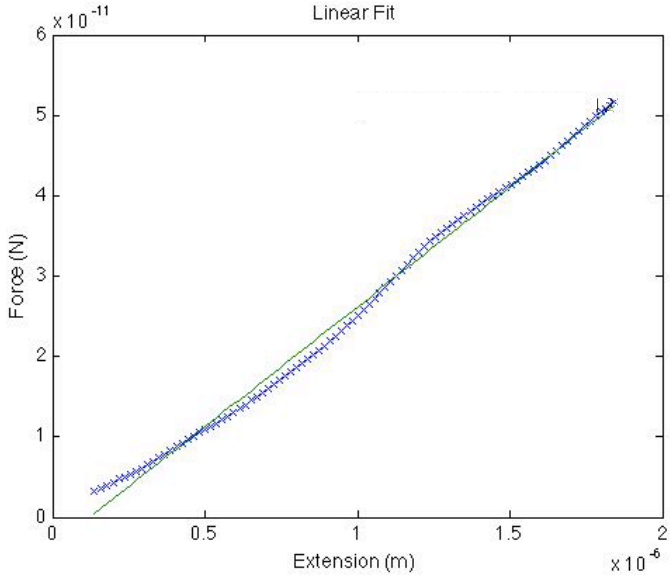

Figure 8.2: A linear function is fitted to the force-extension curve in order to obtain the spring constant κ_t for the tether. Data from 28.04.08.

For data recorded before 14/05, the procedure described above was a bit different, because the voltage signal was negative compared to the positive V_x. This meant that the second sign in eq. 8.1.1 must be negative, as well as the first term in eq. 8.1.2. Except for

these corrections, the program was run as for data recorded after 14/5.

The range used for the linear fit was variable. Each curve was assessed before deciding which part of it should be fitted. There are several reasons not to fit to the whole range. First of all, the bead in the trap was often placed slightly away from the site where the tether was attached to the bacterium. If the bead was sitting to the left of the attachment site and the tether was extended to the right, the bead would first have to pass the attachment site before a tether was actually formed. The distance where the bead was moving without sensing any force, or perhaps even sensing a negative force, as the bead might be pushed towards the attachment site, should be left out when calculating the slope of the force-extension curve.

Secondly, the bead might have stuck to impurities in the sample chamber even though measurements were made 2 μm above the surface. This could lead to jolts which influence the slope of the force-extension curve, and the part of the curve where such bumps occur should be left out of consideration.

Thirdly, the bead moved out of the linear area on the QPD mentioned in section 5.3.2 (fig. 8.3) in three measurements. If the part of the signal recorded in this region was not included, the measurements could still be used.

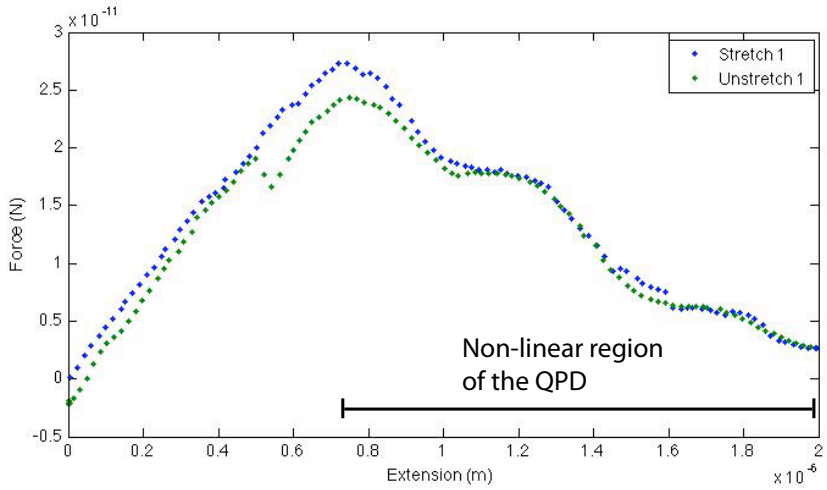

Figure 8.3: Force-extension curve. From 0.7-2.0 μm the laser beam incident on the photodiode is outside the linear region. Data from 05.05.08.

Finally, some tethers broke during measurements (fig. 8.4). If it happened after at least 1 μm, the measurement was still considered to be fit for use, but the part of the curve

where the force dropped to zero was of course not included when fitting.

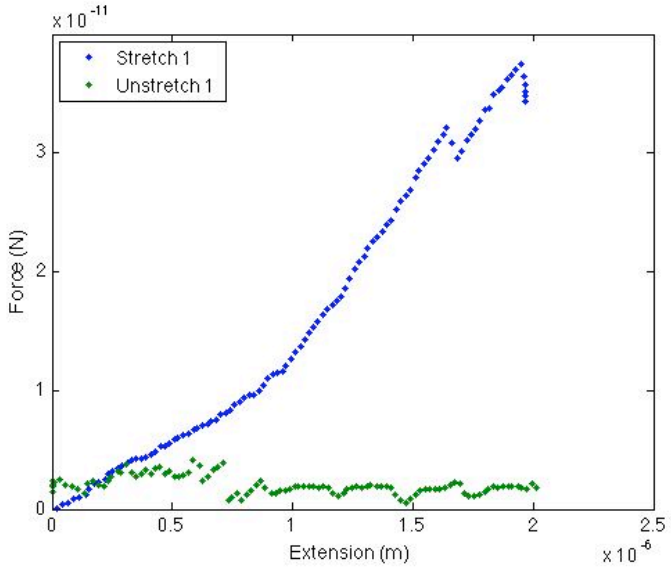

Figure 8.4: The curve shows a tether breaking just before it is fully extended. After the tether is broken, the bead is detached from the membrane and moves along with the trap. Data from 28.04.08.

A last feature of some of the measurements was that the force-extension curve was arched as the one shown in figure 8.5. This was only observed for single measurements both with and without peptide, and since no explanation could be found for the shape of the curves, these measurements were disregarded.

Relaxation

For the relaxation measurements, the force was calculated as described above for the force-extension curves, except that there was no Stoke's drag on the bead when the stage was stationary. Furthermore, the x-axis depicts time instead of extension. The curve was treated as two separate curves, one for extension and one for relaxation (fig. 8.6(a)). The relaxation part was fitted with an exponential function $y = b + a \cdot \exp(\frac{-t}{\tau})$, and to simplify the fitting procedure, this part of the curve was shifted to start at $t = 0$ (fig. 8.6(b)).

8.1.2 Calibration

The data for the movement of the bead in the trap recorded with 'OnlineCalibration3.vi' were processed with the calibration program written by Hansen *et al.* [53] mentioned

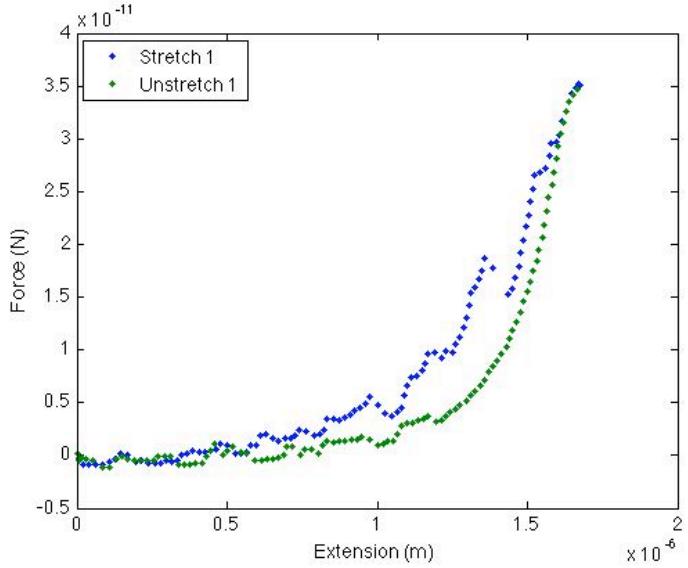

Figure 8.5: Arched curve. Data from 21.05.08.

in section 5.4.3. This program has a graphical user interface where several parameters could be entered. First, the sampling frequency (22 kHz) was given. Then the numbers of the columns containing the movement in the x-direction and the y-direction, respectively, was entered. For data recorded before 14/5 the x channel corresponded to the third column in the data file, and the y channel corresponded to the second column. For data recorded on and after 14/5, the x channel corresponded to the second column and the y channel corresponded to the third column. After the sampling frequency and the column numbers were entered, the data set was checked for cross-talk between the x and the y channel. If the motion in the two directions was not completely independent, some cross-talk emerged, but it was eliminated as described in [58]. Then a histogram of the position of the bead in the two directions was plotted and a Gaussian distribution was fitted to it in order to test if the trapping potential was actually harmonic. This fit also gave the value of σ_{V_x} needed for the calculation of the conversion factor A as described in section 5.4.3. Finally, the theoretical power spectrum was fitted. Several parameters and artefacts could be accounted for when fitting. One artefact is aliasing, an effect arising when the sampling frequency is higher than the Nyquist frequency mentioned in section 5.4.2. Due to the way of calculating the power spectrum, frequencies above the Nyquist frequency will be folded back and added to frequencies below the Nyquist frequency which means that the signal appears to have a lower frequency than is actually the case. Another artefact

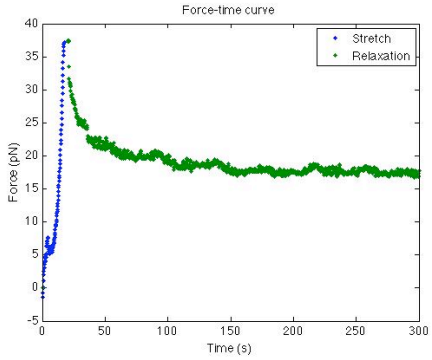

(a) Force vs. time. Measurement is made in the presence of 2 μM arenicin-3.

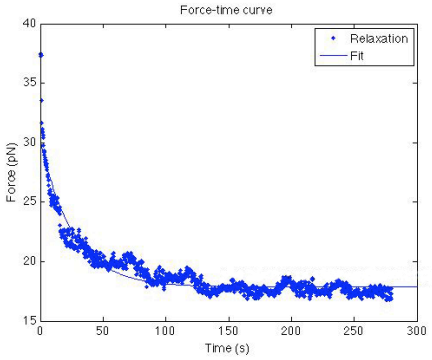

(b) Fit of the relaxation part of the curve.

Figure 8.6: Relaxation curve. Data from 18.05.08.

is unintended filtering by the photodiode system as mentioned in section 5.3.1. Both of these artefacts were taken into consideration when fitting.

Since my measurements were conducted only 2 μm above the surface, it was important to use Faxen's corrections to the Stoke's drag, γ.

Errors and uncertainties

In the data analysis of the force-extension measurements described above, only the force in the x-direction was considered. The y-component of the force was not included, as the motion was expected to be mainly in the x direction. This might not have been completely correct, as the photodiode could have been slightly askew. This would mean that a movement in the x-direction would also have a component in the y-direction. By not accounting for that, the force would seem smaller than it actually was. The y-component, however, only had a small influence on the slope of the force-extension curve, and for simplicity it was not taken into consideration. A much larger error arose from making all measurements 2 μm above the surface. As the bacterium was only ~0.5 μm high, the bead must have been some distance above the bacterium, which means that the tether force would not only be in the x-direction but also have a z-component (fig. 8.7).

The z-component was not measured and was therefore not taken into consideration. This naturally gave rise to an error on the force measurements as the force appeared to be smaller than it actually was. However, the trap is relatively soft in the z-direction, which means that the bead might have been positioned below the centre of the trap. Furthermore, θ was decreasing as the tether was extended, and this made the force in the z-direction even smaller. I tried to conduct all the measurements at the same height, which should

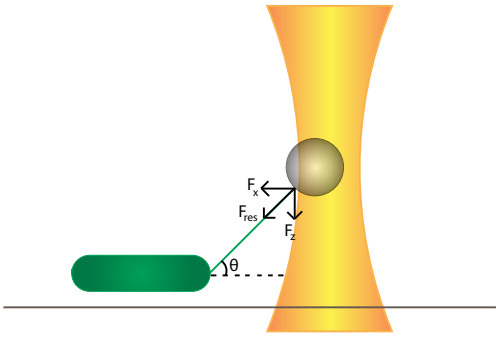

Figure 8.7: When pulling tethers 2 μm above the surface, the force from the tether can be split into two components, one in the x-direction and one in the z-direction.

mean that the relative size of the force in the z-direction would be the same for all measurements, as the relation between force and extension is linear. There was an uncertainty in the height, however, which means that the relation between the force in the z- and the x-direction was not constant.

The calibration measurements also contained some sources of uncertainty. First of all, the height of the bead was not known precisely. Secondly, there was an uncertainty on the bead size of approximately 10%. Both of these factors influenced the value of f_c obtained from the power spectrum and thereby affected the calculation of the force in the data analysis. An uncertainty of 10% on the bead size leads to an uncertainty of approximately 1.5% on f_c, and an uncertainty of 1 μm in the height leads to an uncertainty of approximately 15%.

8.2 Results

In this section I will describe the results I have obtained during my work. First, I will discuss the oscillations mentioned in section 8.1.1, and then the stiffness of tethers measured in the absence of peptide will be compared to the stiffness of tethers in the presence of peptide. Finally, the characteristic time of the relaxation measurements obtained will be discussed.

8.2.1 Oscillations

Several of both the force-extension and the relaxation measurements exhibited regular oscillations with a period of approximately 2 and 40 seconds, respectively, as illustrated by figure 8.8.

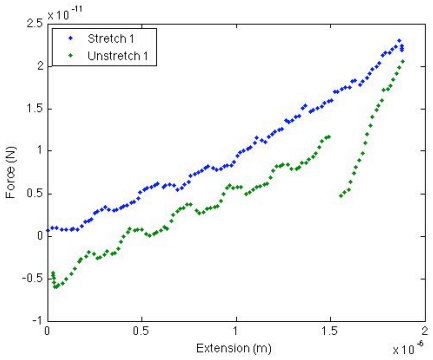

(a) Force-extension curve showing oscillations with a characteristic period of 2 s. Tether is pulled in the presence of 1 μM arenicin-3. Data from 09.04.08.

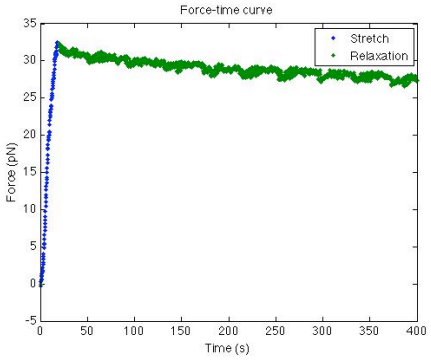

(b) Relaxation curve showing oscillations with a characteristic period of approximately 40 s. Tether is pulled in the absence of peptide. Data from 23.04.08.

Figure 8.8: A force-extension curve and a relaxation curve displaying oscillations.

The oscillations seen in the relaxation measurements were on a much larger time scale than those in the force-extension measurements. The oscillations with a period of 2 seconds might be hidden under the longer ones, but they cannot be detected. Since the oscillations in the relaxation measurements occurred both in the presence and absence of peptide, it can be concluded that the effect is not due to peptides.

The oscillations in the force-extension measurements are artefacts and are not thought to stem from any tether characteristics. This conclusion is build on several factors. Firstly, the oscillations were also observed in measurements in chambers containing only beads and water. Secondly, the oscillations were also seen after tethers broke during measurements and the tether no longer existed. Several tests were made to check if the stage or the laser beam could cause the behaviour.

The stage was checked by trapping a bead stuck to the surface with OT and seeing if any oscillations occurred when moving the trap over the bead (fig. 8.9). The bead was 1.26 μm in diameter, and the stage was moved 10 μm.

No oscillations were observed when scanning over the bead with velocities between 0.05 μm/s and 0.5 μm/s, but on both sides of the bead where the laser only hit the microscope slide, similar oscillations could be seen. The experiment, however, did not clarify whether the oscillations stemmed from the stage or the laser and therefore, the laser was also checked.

The laser was tested by simply recording a power spectrum of the laser beam on the surface of the microscope slide. The piezo stage was turned off to make sure that it did not influence the measurements, and a power spectrum was recorded for 3 seconds in

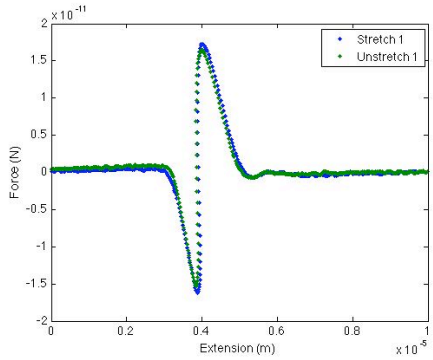

(a) The laser beam is moved over a bead stuck to the surface of a glass slide with a velocity of 0.1 μm/s.

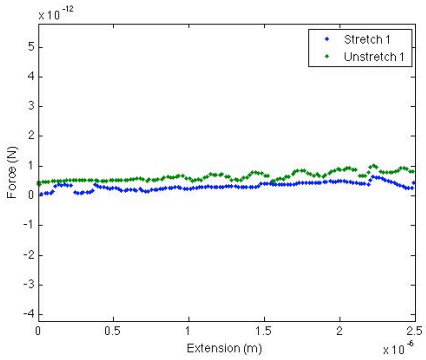

(b) Zoom of the curve from 0 to 2.5 μm.

Figure 8.9: Test of the piezo stage.

both the x-, y-, and z-direction. This time span was much to short in comparison to the observed period, however, and nothing could be concluded on the basis of the test either.

After the two tests were performed, we discovered that 'constantspeed1.vi' had been run with a waiting time of 5 seconds. The waiting time determines how long the stage waits between every step, and if it is in the order of seconds, it will lead to visible steps in the measured curves, thus explaining the oscillations observed. The reason why these steps were not observed in all measurements was probably that they were blurred by drift. The oscillations in the relaxation measurements are thought to have the same cause as the time-scale is also of the order of seconds. The reason for the longer period might lay in another undetected setting in 'constantspeed1.vi'.

The oscillations in the force-extension measurements were simply removed by smoothening the stretching data with a sliding window. As mentioned earlier, only the stretching data was used when calculating the tether stiffness and therefore the unstretch data was not smoothened.

When a sliding window of size 12000 points had been applied, the stretch curve shown in figure 8.8 was transformed into the stretch curve shown in figure. 8.10.

The size of the sliding window was chosen to be 12000 points because this is slightly above the period of the oscillations, which is 5 kHz $\cdot$ 2 seconds = 10000 points.

8.2.2 Force-extension measurements

Table 8.1 contains the results for the tether stiffness obtained from fitting a linear function to the force-extension measurements.

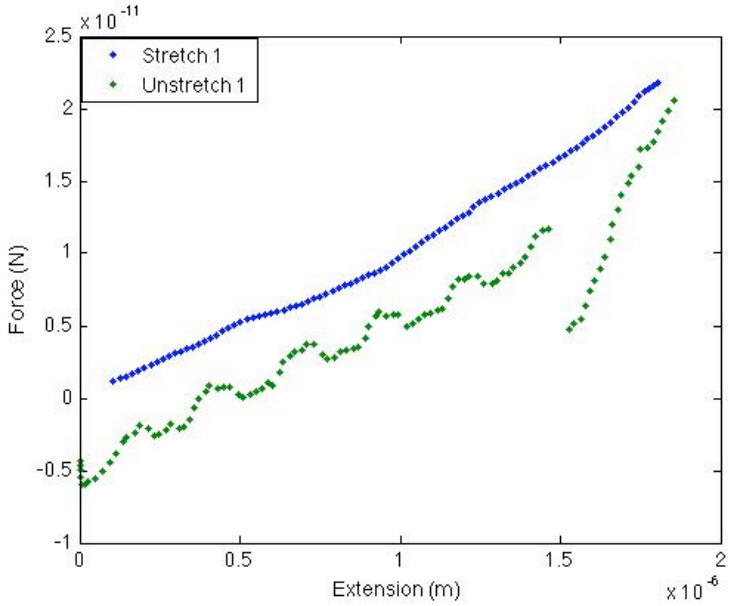

Figure 8.10: Force-extension curve showing smoothened stretching data an untreated unstretching data. Data from 09.04.08.

No experiments were conducted with plectasin. It was deselected because of its high MIC against *E. coli*, and because it in [20] has been stated to have an immeasurable effect on the bacteria.

The results in table 8.1 are given as the mean ± standard deviation in units of pN/μm, and N corresponds to the number of measurements. All measurements were performed with a pulling velocity of 0.1 μm/s.

Table 8.1: Tether stiffness obtained from the force-extension measurements. All values have the unit of pN/μm.

Type	κ_t first pull	κ_t last pull	κ_t all pulls
SB	21.9 ± 9.8 (N=8)	21.4 ± 11.1 (N=7)	22.8 ± 9.8 (N=19)
Arenicin-3	39.2 ± 10.7 (N=2)	21.5 ± 6.7 (N=5)	26.5 ± 9.9 (N=9)
Novispirin variant	14.3 ± 7.9 (N=5)	35.5 ± 9.9 (N=3)	22.2 ± 13.6 (N=8)

The values of κ_t were divided into three categories: First pull, last pull, and all pulls. The so-called 'first pull' tethers are, as the name suggests, tethers pulled from a bacterium for the first time. If the tether was extended more than one time, the value of the spring constant obtained from the last pull was counted in the last pull-category. Finally, all

the values obtained were evaluated together, including several spring constants for single tethers. The reason for dividing the spring constants into first pull values and last pull values is that the peptides might not influence the membrane tether immediately but only after several consecutive pulls. By comparing the values in the two categories, such an effect could be revealed. Furthermore, there might be a difference between the tether stiffness for first and last pull tethers within the different types of experiments due to relaxation as shown by Jauffred *et al.* [23].

First pull The spring constants obtained for SB were compared to those obtained for arenicin-3 and the novispirin variant using Student's t-test. The t-test investigates whether two data sets are independent random samples from normal distributions with equal means or different means. The t-test was run with a significance level of 5% and under the assumption that the two data sets do not have the same variance.

When comparing the first pull spring constants for SB and arenicin-3, Student's t-test gave p = 0.2164. When comparing the spring constants for SB and the novispirin variant, the t-test gave p = 0.1570. Both p-values exceeded the significance level of p = 0.05, which means that the data sets cannot be concluded to have different mean values. In other words, the peptides apparently have no effect on the tether stiffness for the first pull tethers.

The tether stiffness obtained for first pull tethers by Jauffred *et al.* is (11.6 ± 3.5) pN/μm [40], which is in the same order of magnitude as the value of 21.9 ± 9.8 obtained from my experiments.

Last pull The same test was performed on the last pull tethers, but again, the p-values obtained when comparing the different data sets were much larger than the significance level. The p-value found when comparing SB and arenicin-3 was 0.6853, and for SB and the novispirin variant it was 0.1124. Thus it cannot be concluded that the spring constants for last pull tethers are different in the presence and absence of peptide.

The last pull tethers were also compared to the first pull tethers in the absence of peptide and in the presence of arenicin-3, respectively. This was done with a slightly different test, namely the paired t-test. The paired test was chosen because there is a large deviation between the different values of the tether stiffness in each category. Therefore, only tethers which were pulled several times, and where both the first pull value and a last pull value were obtained, were used. The paired t-test was only performed on the data set for SB and arenicin-3 because only one tether was pulled several times in the presence of the novispirin peptide. The result of the paired t-test once more showed that no difference

can be assumed. This indicates that the peptides do not influence the tether stiffness even after several pulls, and it also suggests that no relaxation of the tethers took place during consecutive pulls. This assumption rests on a fragile foundation, however, as the number of measurements is quite small. 6 tethers were pulled several times without peptide, and 4 tethers were pulled several times in the presence of arenicin-3. The result might have been different it the data set had been larger.

The tether stiffness for last pulls obtained by Jauffred *et al.* is (5.7 ± 1.2) pN/μm for the SB strain [40], which is again in the same order of magnitude as the value of (21.4 ± 11.1) pN/μm I obtained.

All pulls The column containing all measurements was used for a second comparison of the experiments with and without peptide, as the sample size is bigger, and the uncertainty therefore is smaller. When performing the Student's t-test it was again revealed that the tether stiffness cannot be concluded to differ when comparing SB with arenicin-3 and the novispirin variant, respectively. Comparing all pulls in the absence of peptide with all pulls in the presence of arenicin-3 gave a p-value of 0.3705, and comparison with the novispirin variant gave a p-value of 0.9127.

In general, the typical forces reached during force-extension measurements lie in the range from 20-30 pN, and the laser power at the laser was 1-1.4 W, of which only approximately 20% reached the sample.

For all experiments conducted, the curve for unstretching lies below the curve for stretching, even though both curves have approximately the same slope. This feature indicates that some hysteresis exists in the system, which is not surprising as the tethers are not completely elastic but also have some viscous properties.

Even though the tethers in the measurements were only pulled 2 μm away from the bacterium, tethers up 10-15 μm long have been observed. As the tethers cannot be seen in the microscope, the diameter must be smaller than ~200 nm.

8.2.3 Relaxation relations

Relaxation curves were only obtained for tethers in the absence of peptide and in the presence of arenicin-3. The relaxation part of both categories of measurements seems to obey a Maxwell-like relaxation, which reveals the viscous properties of the membrane. The relaxation happens with a characteristic time τ which describes how long it takes for membrane material to flow into the tether. If the membrane was purely viscous, like the soap film discussed in section 4.1, the force would eventually relax to zero. This was

not the case for the bacterial tethers, which instead were seen to relax to a force plateau (fig. 8.12). The characteristic time for the relaxation, τ, and the value of the plateau force was found by fitting each measurement with an exponential function $y = b + a \cdot \exp(\frac{-t}{\tau})$ as described in section 8.1.1. Here b corresponds to the value of the force plateau.

All relaxation measurement lasted 300 seconds, and the fitting procedure was done for both 100 and 300 seconds. The fitting range had a very large influence on the values of τ, as can be seen in figure 8.11. The fit with fitting range 100 s has a value of τ equal to 44.3 s, and the fit with fitting range 300 s has a value of τ equal to 175.0 s.

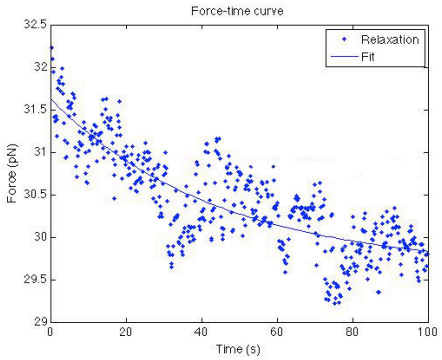

(a) An exponential function is fitted to the relaxation part of the curve shown in fig. 8.8(b). Fitting range is 100 seconds, and τ = 44.3 s.

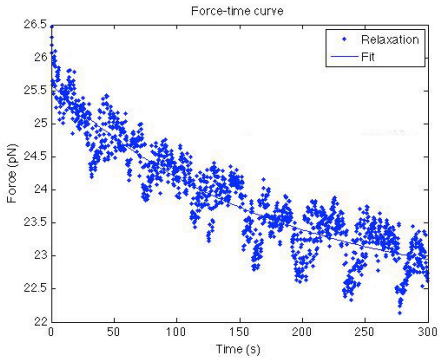

(b) The same curve is fitted for 300 seconds, and τ = 175.0 s.

Figure 8.11: The fitting range for the exponential fit influences the relaxation time.

The fitting range of 300 seconds was estimated to give the best fit for all curves, and thus the τ values obtained with the long fitting range were used for comparison. Table 8.2 shows the values of τ and the plateau force found from the relaxation measurements. All measurements were performed on different tethers.

Table 8.2: Relaxation time τ obtained from the relaxation measurements.

Type	τ	$\langle\tau\rangle \pm$ std	Plateau force $\pm$ std
SB	175.0 s 49.1 s 177.3 s 199.6 s 164.8 s	(153.2 ± 59.5) s	(19.9 ± 12.3) pN
Arenicin-3	25.0 s 26.2 s	(25.6 ± 0.8) s	(14.4 ± 4.9) pN

The relaxation time for tethers in the presence of arenicin-3 appears to be much smaller than the relaxation time for tethers in the absence of peptide. The difference is also clearly visible when comparing two representative relaxation curves in the presence and absence of peptide, respectively (fig. 8.12).

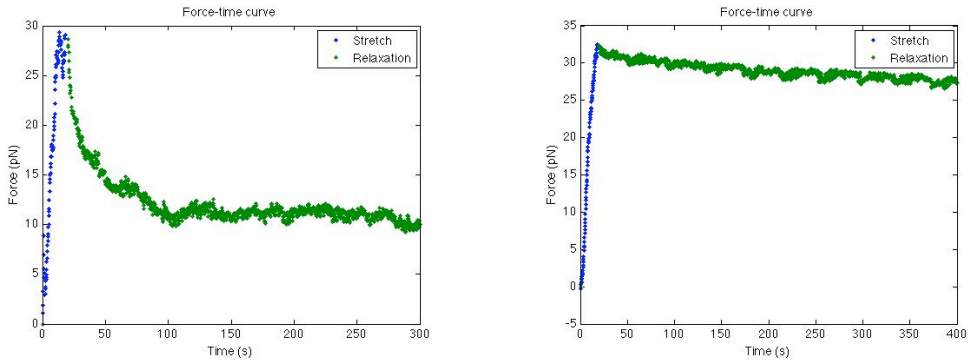

(a) Relaxation measurement in the presence of 2 μM arenicin-3. τ = 25.0 s.

(b) Relaxation measurement in the absence of peptide. τ = 175.0 s.

Figure 8.12: Comparison of two relaxation measurements, the left with 2 μM arenicin-3 present and the right with no peptide present.

The two curves both reach approximately 30 pN during the extension phase, but the tether in the presence of arenicin-3 relaxes much faster and to a lower force than the tether with no peptide present. The force plateau for the arenicin-3 measurement is 10.9 pN, while it is 22.4 pN for the SB measurement.

The sample size is very small, and the numbers in each group might be similar by chance. The difference between the two groups of relaxation times, however, is quite large and is considered to be representative. The values of the force plateau were also compared with Student's t-test, but with a p-value of 0.7388 they are not significantly different.

The values for τ and the force plateau has earlier be found to be (207 ± 117) s and (17.7 ± 2.4) pN, respectively [40], and for other cell types, the characteristic time is found to be 50 s for outer hair cells [29], 1 s for neutrophils [39], and 86 s for vesicles [59].

8.3 Discussion

The results for the force-extension measurements presented in the previous section indicate that arenicin-3 and the novispirin variant do not have any effect on the tether stiffness. It cannot be completely ruled out that the peptides do influence the tether stiffness, however. The effect might just be so small that it is concealed by the uncertainty on the

measurements. This seems a reasonable possibility, especially as arenicin-3 appears to have a quite large effect on the relaxation time τ obtained from the relaxation measurements. This result is of course also based on a very small sample size, but the values of τ are definitely different and have relatively small standard deviations.

The effect of arenicin-3 on τ can be explained by the SHM model. In the model the peptides mainly affect the inner membrane without necessarily destroying the outer membrane completely. In order to reach the inner membrane, however, the model proposes that cationic antimicrobial peptides create cracks in the outer membrane of Gram-negative bacteria by neutralising the negatively charged membrane as described in section 3.2.2. When cracks occur, the LPS leaflet becomes less tightly bound together, and lipids can more easily flow into the tether. Such cracks will not necessarily influence the force-extension measurements, as the time scale in these experiments is much shorter.

The novispirin variant is more cationic than arenicin-3, and thus it could be expected to affect the relaxation measurements even more than arenicin-3, if the explanation above is correct.

Chapter 9

Conclusion

Force-extension measurements and relaxation measurements have been carried out in order to see whether three different antimicrobial peptides influence the outer membrane of *E. coli* bacteria.

Force-extension measurements were performed with no peptide present and in the presence of arenicin-3 and a novispirin variant, respectively. Tethers were pulled 2 μm away from the bacterium with a speed of 0.1 μm/s. All measurements obey Hooke's law $F = \kappa \cdot x$, where κ denotes the tether stiffness. The value of the tether stiffness obtained for tethers without peptide present is κ_{SB} = (22.8 ± 9.8) pN/μm. This value is on the same order of magnitude as the value of (7.7 ± 2.7) pN/μm found in [40]. In the presence of arenicin-3, the value is $\kappa_{arenicin-3}$ = (26.5 ± 9.9) pN/μm, and with the novispirin variant, the tether stiffness is $\kappa_{novispirin}$ = (22.2 ± 13.6) pN/μm. The different values of the tether stiffness were compared to each other using Student's t-test. The t-test showed that the values were not significantly different from each other. First pull tethers and last pull tethers were also compared to see if a relaxation took place when pulling the tethers several times and whether the peptides only influenced the tethers after several pulls. The t-test indicated that the first pull values were not different from the last pull values. This result suggests that the peptides do not influence the tether stiffness, not even after the tether has been pulled several times. Furthermore, the result indicates that no relaxation takes place during several consecutive pulls. The last result is not in agreement with the results obtained by Jauffred [40], where a relaxation is seen to take place after a number of pulls. However, the discrepancy is most likely due to the large error bars on my experiments.

Relaxation measurements, where a tether is pulled to 2 μm away from the bacterium and held there for 280 s, showed a pronounced difference in the characteristic relaxation time τ for experiments with no peptide present and experiments with arenicin-3. The

characteristic time for measurements with no peptide present is (τ_{SB} = 153 ± 59.5) s, which agrees with the value of (207 ± 117) s found in [23]. The relaxation time for tethers in the presence of arenicin-3 is (25.6 ± 0.8) s, which is significantly different from τ_{SB}. No effect is seen on the plateau force, however.

The results from the relaxation measurements suggest that arenicin-3 has an influence on the membrane tethers, even though it is not apparent from the force-extension measurements. The results might be explained by the Shai-Matsuzaki-Huang model for peptide action, which suggests that peptides create cracks in the outer membrane. When cracks occur, the LPS leaflet becomes less tightly bound together, and lipids can more easily flow into the tether. It cannot be determined whether the toroidal pore model or the carpet model describes the action of the peptides on the inner membrane, as optical tweezers can only measure characteristics of the outer membrane according to the model for Gram-negative tethers by Jauffred *et al.* [23].

The measurements performed in this thesis are interesting from a pharmaceutical point of view, because experiments with peptides so far mainly have been conducted *in vitro* and not on living cells. Since living microbes are the target of antimicrobial peptides, it is important to know exactly how the peptides attack these organisms in order to be able to optimise the peptide structure.

9.1 Outlook

In order to gain more insight into the effect of the antimicrobial peptides discussed in this thesis, more experiments, both relaxation and force-extension measurements, should be performed with arenicin-3 and the novispirin variant to obtain a larger sample size. It would in particular be interesting to see if the novispirin variant would have any effect on the relaxation time of the tethers, as this might support the SHM model. Another experiment that could shed light on the peptides mechanism of action would be to increase the tether length and see if the tethers would then be influenced by the peptides.

Furthermore, pulling a tether to a certain length, waiting for some time, and then pulling the tether even further might give even more information about the relaxation relation, both in the presence and absence of peptides.

Appendices

Appendix A

Protocols

A.1 Growing *E. coli* bacteria

The SB strain S2188 used for experiments was kept in a sugar solution (B.1) and stored at -80°C in Eppendorf tubes. The strain was genetically modified so that it is resistant to the ampenicillin chloramphenicol (CAM). By growing SB on an agar plate containing CAM, it was assured that no other bacteria survived on the plate.

E. coli bacteria were grown by transferring a small amount of bacteria from the Eppendorf tube to a YT-CAM agar plate (B.2). YT is a rich growth medium containing yeast extract and tryptone. The bacteria were then spread out with an inoculation needle and incubated at 37°C for 12-16 hours. When the colonies reached a proper size, the YT-CAM plate was transferred to the refrigerator where the growth process of the bacteria was halted. It was important that the colonies did not grow so big that they melted together. This was to assure that the colony chosen for experiments had plenty of nutrition and was as healthy as possible. The day before experiments were carried out, a single colony of bacteria was transferred to a conical flask containing 3 mL of M63 growth medium with glycerol (B.3). The flask was then put in a heating bath at 37°C for 12-16 hours overnight. 0.1 mL of this solution was mixed with another 3 mL of M63 with glycerol and left in the heating bath for 1.5 hours. In this time span the bacteria were in the so called logarithmic growth phase. This is a phase of exponential growth where mutations are at a minimum. The fresh M63 should be at least room temperature before the bacteria were added. Otherwise they suffered a cold shock and the lag phase, i.e. the inactive phase before the exponential growth phase where the bacteria adapt to the new conditions, was prolonged. After 1.5 hours, 1 mL of the solution was transferred to an Eppendorf tube and spun down at 5000 rpm for 4 minutes. The supernatant was removed and the bacteria were re-suspended in approximately 200 μL buffer (B.6).

A.2 Washing and coating of polystyrene beads

Before coating, the beads (polystyrene, Bangs Laboratories, Inc.) were washed in order to remove surfactants. In this procedure it was important that the water was extremely clean. Otherwise the hydrophobic beads would simply attract all impurities from the water [60]. The washing and coating procedure applied to both sizes of beads and was as follows:

25 μL beads were mixed with 975 μL millipore water in an Eppendorf tube and centrifuged at 4000 rpm for 4 minutes. The supernatant was removed, and the beads were re-suspended in 50 μL PBS-buffer (B.5) and 10 μL lectin (0.1 mg/mL). 10 μL BSA (10 mg/mL) was added to the solution to prevent the beads from forming agglomerates and to fill the binding sites not occupied by lectin [61]. The Eppendorf tube was oscillated for 2 hours at room temperature as described in [62].

After coating, the beads were washed several times to remove the excess lectin and BSA. The washing procedure was the same as that used before coating the beads, i.e. 930 μL PBS was added so that the volume reached a total of 1 mL, and the beads were spun down at 4000 rpm for 4 minutes. Then the supernatant was removed, the beads were re-suspended in 1000 μL PBS and centrifuged again at 4000 rpm for 4 minutes. This process was repeated two more times, so that the beads were washed three times in total. After the last centrifugation, the beads were re-suspended in approximately 300 μL PBS, depending on a visual estimate of how many beads were left after the washing procedure.

A.3 Preparation of sample chambers

Perfusion chambers were made of a large glass microscope slide of 24x50 mm, two pieces of double-layered, double-sided tape, and a small glass cover slip of 18x18 mm. 10 μL 2% poly-l-lysine was spread on a cleaned large slide and was left to dry. Poly-l-lysine is a highly positively charged amino acid chain that promotes cell adhesion. It is not known whether the poly-l-lysine influences tether formation, and therefore the layer on the cover-slide was made as thin as possible. When the liquid had dried, the two pieces of double-layered, double-sided tape were stuck to the glass slide in such a manner that they formed a channel approximately 2-3 mm wide (fig. 7.1). The small cover slip was placed on top of the tape in order to form a lid. The volume of the chamber was approximately 10 μL.

A.3.1 Perfusion

Chambers were washed with 40 μL millipore water and perfused with 18 μL of the bacteria-buffer solution. After that they were left to incubate for 20 minutes. Incubation was always done over a water bath at room temperature in order to prevent the chambers from drying out. Next, the chamber were perfused with 15 μL heparin (12.5 mg/mL) and incubated for 15 minutes. Heparin is extremely negatively charged and is added to prevent the beads from sticking to the surface. Then 40 μL buffer was run through the chamber to remove the heparin and any surplus bacteria, and 18 μL of beads were perfused into the chamber and left to incubate for another 20 minutes. Finally, the chamber was washed with 30-60 μL M63 with glucose (B.4), depending on the amount of beads in the chamber, and sealed with vacuum grease. The reason why the growth medium in this last step contained glucose and not glycerol was that *E. coli* bacteria can only digest glycerol in aerobic environments. In anaerobic environments, glucose must be used as nutrition instead.

When preparing samples with peptide, 10 μl peptide at a concentration of 2 μM were added just before sealing the chambers.

Appendix B

Recipes

B.1 Bacteria stabs

The bacterial strain is spread on a YT-CAM agar plate.
The plate is incubated at 37 °C overnight.
A single colony from the plate is transferred to a conical flask with 3 ml medium, and the flask is put in a shaking bath at 37°C for 10-16 hours (overnight).
A 50% $\frac{w}{v}$ glycerol mixture is prepared by putting 50 g glycerol in a 100 ml bottle. Millipore water is added up to the 100 ml mark. The mixture is autoclaved and cooled.
1 ml of the overnight culture is mixed with 0.8 ml glycerol mixture and is frozen immediately (-80°C).

B.2 YT-CAM medium

- 250 ml of millipore water
- 2.5 g NaCl
- 4.0 g tryptone
- 2.5 g yeast extract
- 7.5 g agar
- The ingredients are mixed well and an additional amount of 250 ml millipore water is added
- The mixture is autoclaved and then shaken very rigourously while it is still hot

- The mixture is cooled to approximately 60°C
- Chloramphenicol (CAM) is added to a final concentration of 25 μg/ml, and the mixture is stirred gently to avoid the formation of air bubbles.

B.3 M63 medium with glycerol

- 40 ml millipore water
- 10 ml 5X M63
- Solution is autoclaved and cooled
- 0.5 ml 20% glycerol
- 0.25 ml 20% CAA
- 0.05 ml 1M $MgSO_4$
- 0.05 ml B1 MIX
- 0.05 ml CAM
- All ingredients are transferred sterilely, and the final mixture is sterilely filtered.

B.4 M63 medium with glucose and EDTA

- 40 ml millipore water
- 10 ml 5X M63
- 0.5 ml 20% glucose
- 0.25 ml 20% CAA
- 0.05 ml B1 MIX
- 0.05 ml CAM
- 0.1 ml 0.5M EDTA
- All ingredients are transferred sterilely, and the final mixture is sterilely filtered.

B.5 PBS buffer, pH 7

- 1M Na_2HPO_4 (stock 1):

  1,42 g Na_2HPO_4 dissolved in 10 ml H_2O

- 1M NaH_2PO_4 (stock 2):

  1,19 g NaH_2PO_4 dissolved in 10 ml H_2O

- 0.1M PO_4 , pH 7 (stock 3):

  5.77 ml stock 1

  4.23 stock 2

  90 ml H_2O

- 20 ml stock 3
- 0.88 g NaCl
- Add H_2O to a total of 100 ml
- Check pH.

B.6 Phosphate buffer

- Potassium phosphate is mixed with millipore water to a concentration of 10 mM
- KCl is added to a concentration of 0.1 M

Bibliography

[1] B. Beutler and R. Meganathan. Biosynthesis of vitamin K (menaquinone) in bacteria. *Microbiol. Mol. Biol. Rev.*, 46(3):241–280, 1982.

[2] Wikipedia. Peptidoglycan — wikipedia, the free encyclopedia, 2008. `http://en.wikipedia.org/w/index.php?title=Peptidoglycan&oldid=214837054`.

[3] R. Bentley and E.T. Rietschel. Innate immune sensing and its roots: the story of endotoxin. *Nat Rev Immunol*, 3(2):169–176, 2003.

[4] C.R.H. Raetz, C.M. Reynolds, M.S. Trent, and R.E. Bishop. Lipid a modification systems in gram-negative bacteria. *Annual Review of Biochemistry*, 76(1):295 – 329, 2007.

[5] `http://www.bact.wisc.edu/themicrobialworld/Structure.html`.

[6] Y. Shai. Mechanism of the binding, insertion and destabilization of phospholipid bilayer membranes by α-helical antimicrobial and cell non-selective membrane-lytic peptides. *Biochimica et Biophysica Acta (BBA) - Biomembranes*, 1462(1-2):55–70, 1999.

[7] K. Matsuzaki. Why and how are peptide-lipid interactions utilized for self-defense? magainins and tachyplesins as archetypes. *Biochimica et Biophysica Acta (BBA) - Biomembranes*, 1462(1-2):1–10, 1999.

[8] M. Zasloff. Antimicrobial peptides of multicellular organisms. *Nature*, 415(6870):389–395, 2002.

[9] L. Yang, T.M. Weiss, R.I. Lehrer, and H.W. Huang. Crystallization of Antimicrobial Pores in Membranes: Magainin and Protegrin. *Biophys. J.*, 79(4):2002–2009, 2000.

[10] J.S. Powers and R.E.W. Hancock. The relationship between peptide structure and antibacterial activity. *Peptides*, 24(11):1681–1691, 2003.

[11] B. Bechinger and K. Lohner. Detergent-like actions of linear amphipathic cationic antimicrobial peptides. *Biochimica et Biophysica Acta (BBA) - Biomembranes*, 1758(9):1529–1539, 2006.

[12] A. Tossi, L. Sandri, and A. Giangaspero. Amphipathic, α-helical antimicrobial peptides. *Biopolymers*, 55(1):4–30, 2000.

[13] T. Ganz. Defensins: antimicrobial peptides of innate immunity. *Nat Rev Immunol*, 3(9):710–720, 2003.

[14] S. Ludtke, K. He, and H. Huang. Membrane thinning caused by magainin 2. *Biochemistry*, 34(51):16764–16769, 1995.

[15] H. Huang. Action of antimicrobial peptides: Two-state model. *Biochemistry*, 39(29):8347–8352, 2000.

[16] K. A. Brogden. Antimicrobial peptides: pore formers or metabolic inhibitors in bacteria? *Nat Rev Micro*, 3(3):238–250, 2005.

[17] C. Hetru, L. Letellier, Z. Oren, J.A. Hoffmann, and Y. Shai. Androctonin, a hydrophilic disulphide-bridged non-haemolytic anti-microbial peptide: a plausible mode of action. *Biochem. J.*, 345:653–664, 2000.

[18] M.W. Maddox and M.L. Longo. A Monte Carlo Study of Peptide Insertion into Lipid Bilayers: Equilibrium Conformations and Insertion Mechanisms. *Biophys. J.*, 82(1):244–263, 2002.

[19] D. Shental-Bechor, T. Haliloglu, and N. Ben-Tal. Interactions of Cationic-Hydrophobic Peptides with Lipid Bilayers: A Monte Carlo Simulation Method. *Biophys. J.*, 93(6):1858–1871, 2007.

[20] P.H. Mygind, R.L. Fischer, and K.M. Schnorr. Plectasin is a peptide antibiotic with therapeutic potential from a saprophytic fungus. *Nature*, 437(7061):975–980, 2005.

[21] L. Steinstraesser, B.F. Tack, A.J. Waring, T. Hong, L.M. Boo, M. Fan, D.I. Remick, G.L. Su, R.I. Lehrer, and S.C. Wang. Activity of Novispirin G10 against Pseudomonas aeruginosa In Vitro and in Infected Burns. *Antimicrob. Agents Chemother.*, 46(6):1837–1844, 2002.

[22] R. Wimmer, K.K. Andersen, B. Vad, M. Davidsen, S. Molgaard, L.W. Nesgaard, H.H. Kristensen, and D.E. Otzen. Versatile interactions of the antimicrobial peptide novispirin with detergents and lipids. *Biochemistry*, 45(2):481–497, 2006.

[23] L. Jauffred, T.H. Callisen, and L. B Oddershede. Visco-Elastic Membrane Tethers Extracted from Escherichia coli by Optical Tweezers. *Biophys. J.*, 93(11):4068–4075, 2007.

[24] T.R. Powers, G. Huber, and R.E. Goldstein. Fluid-membrane tethers: Minimal surfaces and elastic boundary layers. *Phys. Rev. E*, 65(4):041901, 2002.

[25] D.K. Fygenson, J.F. Marko, and A. Libchaber. Mechanics of microtubule-based membrane extension. *Phys. Rev. Lett.*, 79(22):4497–4500, 1997.

[26] E. Evans and A. Yeung. Hidden dynamics in rapid changes of bilayer shape. *Chemistry and Physics of Lipids*, 73(1-2):39–53, 1994.

[27] S. Svetina, B. Zeks, R.E. Waugh, and R.M. Raphael. Theoretical analysis of the effect of the transbilayer movement of phospholipid molecules on the dynamic behavior of a microtube pulled out of an aspirated vesicle. *Eur Biophys J*, 27(3):197–209, 1998.

[28] G. Koster, A. Cacciuto, I. Derenyi, D. Frenkel, and M. Dogterom. Force barriers for membrane tube formation. *Physical Review Letters*, 94(6):068101, 2005.

[29] Z. Li, B. Anvari, M. Takashima, P. Brecht, J.H. Torres, and W.E. Brownell. Membrane Tether Formation from Outer Hair Cells with Optical Tweezers. *Biophys. J.*, 82(3):1386–1395, 2002.

[30] D. Raucher and M.P. Sheetz. Characteristics of a Membrane Reservoir Buffering Membrane Tension. *Biophys. J.*, 77(4):1992–2002, 1999.

[31] J. Dai and M.P. Sheetz. Mechanical properties of neuronal growth cone membranes studied by tether formation with laser optical tweezers. *Biophys. J.*, 68(3):988–996, 1995.

[32] W.C. Hwang and R.E. Waugh. Energy of dissociation of lipid bilayer from the membrane skeleton of red blood cells. *Biophys. J.*, 72(6):2669–2678, 1997.

[33] W.D. Marcus and R.M. Hochmuth. Experimental Studies of Membrane Tethers Formed from Human Neutrophils. *Annals of Biomedical Engineering*, 30(10):1273–1280, 2002.

[34] D.W. Schmidtke and S.L. Diamond. Direct Observation of Membrane Tethers Formed during Neutrophil Attachment to Platelets or P-selectin under Physiological Flow. *J. Cell Biol.*, 149(3):719–730, 2000.

[35] R.M. Hochmuth, C.A. Evans, H.C. Wiles, and J.T. McCown. Mechanical measurement of red cell membrane thickness. *Science*, 220(4592):101–102, 1983.

[36] S.A. Ermilov, D.R. Murdock, F. Qian, William E. Brownell, and B. Anvari. Studies of plasma membrane mechanics and plasma membrane-cytoskeleton interactions using optical tweezers and fluorescence imaging. *Journal of Biomechanics*, 40(2):476–480, 2007.

[37] F.M. Hochmuth, J.Y. Shao, J. Dai, and M.P. Sheetz. Deformation and flow of membrane into tethers extracted from neuronal growth cones. *Biophys. J.*, 70(1):358–369, 1996.

[38] E. Evans, V. Heinrich, A. Leung, and K. Kinoshita. Nano- to Microscale Dynamics of P-Selectin Detachment from Leukocyte Interfaces. I. Membrane Separation from the Cytoskeleton. *Biophys. J.*, 88(3):2288–2298, 2005.

[39] V. Heinrich, A. Leung, and E. Evans. Nano- to Microscale Dynamics of P-Selectin Detachment from Leukocyte Interfaces. II. Tether Flow Terminated by P-Selectin Dissociation from PSGL-1. *Biophys. J.*, 88(3):2299–2308, 2005.

[40] Liselotte Jauffred. An investigation of elastic bacterial tethers with optical tweezers. Master's thesis, Niels Bohr Institute, University of Copenhagen, 2006.

[41] R.M. Hochmuth and W.D. Marcus. Membrane tethers formed from blood cells with available area and determination of their adhesion energy. *Biophysical Journal*, 82(6):2964–9, 2002.

[42] A. Ashkin. Acceleration and trapping of particles by radiation pressure. *Phys. Rev. Lett.*, 24(4):156–159, 1970.

[43] A. Ashkin, J.M. Dziedzic, J.E. Bjorkholm, and S. Chu. Observation of a single-beam gradient force optical trap for dielectric particles. *Opt. Lett.*, 11(5):288–290, 1986.

[44] Michael P. Sheetz, editor. *Laser Tweezers in Cell Biology*, volume 55 of *Methods in Cell Biology*. Academic Press, 1998.

[45] G. Roosen and C. Imbert. Optical levitation by means of two horizontal laser beams: A theoretical and experimental study. *Physics Letters A*, 59(1):6–8, 1976.

[46] A. Ashkin. Forces of a single-beam gradient laser trap on a dielectric sphere in the ray optics regime. *Biophys. J.*, 61(2):569–582, 1992.

[47] K. Svoboda and S.M. Block. Biological applications of optical forces. *Annual Review of Biophysics and Biomolecular Structure*, 23(1):247–285, 1994.

[48] A Rohrbach. Stiffness of optical traps: Quantitative agreement between experiment and electromagnetic theory. *Physical Review Letters*, 95(16):168102, 2005.

[49] S.N.S. Reihani and L.B. Oddershede. Optimizing immersion media refractive index improves optical trapping by compensating spherical aberrations. *Opt. Lett.*, 32(14):1998–2000, 2007.

[50] Dejan Trpcevski. Optical stretching of dna as a diagnostic tool in nanotoxicology. Master's thesis, Niels Bohr Institute, University of Copenhagen, 2006.

[51] K. Berg-Sørensen, L.B. Oddershede, E. Florin, and H. Flyvbjerg. Unintended filtering in a typical photodiode detection system for optical tweezers. *Journal of Applied Physics*, 93(6):3167–3176, 2003.

[52] F. Gittes and C.F. Schmidt. Interference model for back-focal-plane displacement detection in optical tweezers. *Opt. Lett.*, 23(1):7–9, 1998.

[53] P.M. Hansen, I.M. Tolic-Nørrelykke, H. Flyvbjerg, and K. Berg-Sørensen. tweezercalib 2.0: Faster version of matlab package for precise calibration of optical tweezers. *Computer Physics Communications*, 174(6):518–520, 2006.

[54] L.B. Oddershede, S. Grego, S.F. Nørrelykke, and K. Berg-Sørensen. Optical tweezers: Probing biological surfaces. *Probe Microscopy*, 2(2):p129 – 137, 2001.

[55] K.C. Neuman, E.H. Chadd, G.F. Liou, K. Bergman, and S.M. Block. Characterization of Photodamage to Escherichia coli in Optical Traps. *Biophys. J.*, 77(5):2856–2863, 1999.

[56] M.B. Rasmussen, L.B. Oddershede, and H. Siegumfeldt. Optical Tweezers Cause Physiological Damage to Escherichia coli and Listeria Bacteria. *Appl. Environ. Microbiol.*, 74(8):2441–2446, 2008.

[57] Stanley Brown. Metal-recognition by repeating polypeptides. *Nat Biotech*, 15(3):269–272, 1997.

[58] I.M. Tolic-Nørrelykke, K. Berg-Sørensen, and H. Flyvbjerg. Matlab program for precision calibration of optical tweezers. *Computer Physics Communications*, 159:225–240, 2004.

[59] R.M. Raphael and R.E. Waugh. Accelerated interleaflet transport of phosphatidylcholine molecules in membranes under deformation. *Biophys. J.*, 71(3):1374–1388, 1996.

[60] L.B Bangs and M. Meza. Microspheres, part 1. *IVD Technology Magazine*, March(5):5, 1995.

[61] L.B Bangs and M. Meza. Microspheres, part 2. *IVD Technology Magazine*, March(5):5, 1995.

[62] H. Guo, C. Liu, J. Duan, Y. Jiang, X. Han, Z. Li, B. Cheng, and D. Zhang. Mechanical properties of breast cancer cell membrane studied with optical tweezers. *Chinese Physics Letters*, 21, 2004.